MODEL-BASED HYBRID FRAMEWORK FOR LIVE LOAD CARRYING PERFORMANCE MONITORING OF BRIDGES

by

Andrew Walcker

Copyright © Andrew Walcker 2017

A Thesis Submitted to the Faculty of the

DEPARTMENT OF CIVIL ENGINEERING AND ENGINEERING MECHANICS

In Partial Fulfillment of the Requirements

For the Degree of

MASTER OF SCIENCE

In the Graduate College

THE UNIVERSITY OF ARIZONA

2017

STATEMENT BY AUTHOR

The thesis titled *Model-based Hybrid Framework for Live Load Carrying Performance Monitoring of Bridges* prepared by *Andrew Walcker* has been submitted in partial fulfillment of requirements for a master's degree at the University of Arizona and is deposited in the University Library to be made available to borrowers under rules of the Library.

Brief quotations from this thesis are allowable without special permission, provided that an accurate acknowledgement of the source is made. Requests for permission for extended quotation from or reproduction of this manuscript in whole or in part may be granted by the head of the major department or the Dean of the Graduate College when in his or her judgment the proposed use of the material is in the interests of scholarship. In all other instances, however, permission must be obtained from the author.

SIGNED: *Andrew Walcker*

APPROVAL BY THESIS DIRECTOR

This thesis has been approved on the date shown below:

Hongki Jo — *11/13/2017*

Professor of Structures — Date

Table of Contents

List of Figures

List of Tables

ABSTRACT

Bridge load rating is a procedure to determine the live load carrying capacity of a bridge. This rating is generally given out on a two-year period, which leaves the structural capacity unknown for this time interval. Conventional bridge load rating is obtained according to the bridge inspection results and commercial bridge rating software. However, this approach cannot effectively reflect actual live load carrying performance of the bridge, due to intrinsic limitation of visual inspection. Structural sensing has been utilized for measuring realistic structural behaviors to reflect the live load carrying capacity. However, this expensive and time-consuming process requires a known-weight vehicle and a substantial number of sensors under controlled full-scale field test conditions. In this research, a continuous live load performance index (LLPI) is proposed to monitor the live load capacity that the bridge can withstand without knowing the vehicle weight while also using a limited number of sensors. The LLPI uses existing bridge load rating methodology, in conjunction with experimental data and numerical simulations, to generate a value that describes the performance of the bridge due directly to the live load applied. Furthermore, the LLPI procedure utilizes an advanced state estimation algorithm, known as the Kalman Filter, to estimate the strain responses of the bridge at various locations while using a limited number of sensors. This procedure allows for an efficient structural health monitoring approach to determine the live load carrying capacity that the bridge can withstand. This research uses a lab-scaled truss structure with known properties for numerical and experimental validation. Because of this, this paper proposes a framework as to which the live load carrying performance can be monitored in real time. Future updates include testing on a real-life bridge structure while also determining optimal sensor placement for obtaining the LLPI. This research looks to develop

a new live load performance index (LPPI) by considering: (1) the benefits and limitations of conventional bridge load rating approach, (2) the system identification and multi-metric data acquisition for the bridge structure, (3) numerical modeling and updating to best reflect the current dynamic properties of the bridge, (4) augmented Kalman Filter to estimate structural responses at various unknown locations, (5) LLPI formulation using experimental data, current bridge load rating methodology, and model-response estimations. The results obtained from this research provide a progressive live load capacity performance template to promote the advancement in civil infrastructure smart monitoring.

1. Introduction

1.1 Bridge Load Rating

The United States infrastructure is deteriorating and insufficient effort is put into monitoring and rehabilitating them. This is evident, as the American Society of Civil Engineers (ASCE) gave the US infrastructure a D+ this previous year (GPA: D, 2017). Bridges are an important contributor to this fact, as approximately 61,000 bridges are compromised; meaning that they are unfit for increasing traffic loads. Many of these bridges are 50+ years old and require constant maintenance (Bad bridges: Federal data shows US infrastructure crumbling, 2014). Detrimental implications result due to bridge failures such as excessive costs for reconstruction or repair and potentially, severe personnel injury.

A load rating procedure was formed to quantify the strength of these bridges subjected to moving traffic loads. The Arizona Department of Transportation (ADOT) fashioned bridge load rating guidelines so that all bridges in Arizona are to be designed and inspected in the same way (ADOT, 2011). ADOT uses a value known as a rating factor (RF), which was created by American Association of State Highway and Transportation Officials (AASHTO), for this purpose. This factor is determined based on the dead load and live load conditions that the bridge is supposed to experiences.

The RF is determined for every member of the structure. The RF ranges from zero to infinity, where any value over one is considered safe. Over time, this RF value can change depending on

many conditions such as the degradation of the bridge, which is generally determined by a visual bridge inspection.

In 1970, AAHSTO created the first inspection manual and it wasn't until the early 1990's where some of the standards used in today's bridge inspection were implemented (Texas Department of Transportation, 2013). Currently, a bridge inspection process occurs on a biennial period to determine the condition of the bridge. During these inspections, the bridge is visually inspected for cracks, corrosion, and other harmful damages. For the inspection process, an NBI rating is given. An inspector visually looks at each member of the bridge and gives a rating from 0 to 9 where a lower number means the element is in poor condition whereas a higher number indicates the member is in good condition. Figure 1.1.1 describes the inspection criteria for the bottom deck of a pretensions bridge. As evident by the chart, the inspection process requires a fair amount of human subjective judgement. This causes discrepancies between inspectors. Furthermore, there are various charts for each element of the bridge structure. Because there are so many charts, it can be difficult to obtain a uniform approach. Bridge inspection is a visual process, so the actual strength of the structure can be misleading. Furthermore, because the inspection happens every 2 years, bridge strength and conditions are unknown in-between this time frame. Structural damages that the bridge experiences will not be reflected until the next inspection period.

Code	Description
N	NOT APPLICABLE. Code N for culverts and other structures without decks, e.g., filled arch bridge, concrete slab, or when covered with false-decking or maintenance sheeting.
9	NEW CONDITION. No noticeable or noteworthy deficiencies which affect the condition of the bottom surface concrete or stay-in-place forms.
8	GOOD CONDITION. Minor cracking less than 1/32" wide (0.8mm) with no spalling, scaling, or delamination. No rust on stay-in-place forms.
7	GOOD CONDITION. Open cracks less than 1/16" wide (1.6mm) at a spacing of 10 ft or more, or light shallow scaling. No rust on stay-in-place forms.
6	FAIR CONDITION. The deck bottom surface has considerable number of open cracks greater than 1/16" wide (1.6mm) at a spacing of 5 ft or less. The bottom surface area exhibits 2% or less of spalled, delaminated, or heavily map cracked areas. Medium scaling on the surface is 1/4" to 1/2" (6.4 mm to 13 mm) in depth. Medium scaling on the surface is 1/4" to 1/2" (6.4 mm to 13 mm) in depth. Stay-in place forms have light surface or freckled rust over less than 2% of the total surface area.
5	FAIR CONDITION. The deck bottom surface area exhibits between 2% and 10% spalled, delaminated, or heavily map cracked areas. There can be excessive cracking in the surface. Heavy scaling 1/2" to 1" in depth (13 mm to 26 mm) can be present. Stay-in place forms have light surface or freckled rust between 2% and 10% of the total surface area.
4	POOR CONDITION. The deck bottom surface area exhibits between 10% and 25% spalled, delaminated, or heavily map cracked areas. Stay-in place forms have light to moderate corrosion over between 10% and 25% of the total surface area. Some small areas may have pulled away exposing the deck concrete.
3	SERIOUS CONDITION. The deck bottom surface is showing advanced deterioration that has seriously affected the primary structural components. Local failures are possible. The bottom surface area exhibits more than 25% spalled, delaminated, or heavily map cracked areas. Structural evaluation and/or load analysis may be necessary to determine if the structure can continue to function without restricted loading or structurally engineered temporary supports. There may be a need to increase the frequency of inspections. Stay-in place forms have moderate to severe corrosion over more than 25% of the total surface area. Some small areas may have pulled away exposing the deck concrete.
2	CRITICAL CONDITION. Deterioration has progressed to the point where the deck will not support design loads and is therefore posted for reduced loads. Emergency deck repairs or shoring with structurally engineered temporary supports may be required by the crews. There may be a need to increase the frequency of inspections. Stay-in place forms have large areas of severe corrosion. Some areas may have pulled away exposing the deck concrete.
1	IMMINENT FAILURE CONDITION. Bridge is closed to traffic due to the potential for deck failure, but corrective action may put the bridge back in service.
0	FAILED CONDITION. Bridge closed. Coordinate with S I & A item 41.

Figure 1.1.1 NBI Rating Chart for Bottom Deck of a Pretension Bridge

AASHTO presented a way to inspect the bridges at any point using nondestructive evaluation (NDE) (AASHTO, 2011). For this method, a truck with a known weight slowly crosses the bridge while strain measurements are recorded. These measurements are utilized with the design data

to determine a new RF value. The NDE method for bridge inspection is beneficial, as it allows for a realistic estimation of the bridge load carrying capacity. However, this method is costly and time consuming. The entire bridge must be shut down for this method to work, which creates traffic disruptions. Because of this, the NDE approach cannot be used on large scale bridges that experience a large volume of traffic, unless the bridge appears to be seriously damaged. An attempt was made to calculate the load rating based on the measured strain in three bridges located in Alabama (Green, 2013). This was successful, as a new RF was calculated utilizing the strain data acquired. However, sensors needed to be placed on all aspects of the bridge that were deemed critical. Furthermore, the sensor location was not optimized and was placed in the assumed areas of maximum stress. This creates a limitation, as not all strain values along the bridge were measured. Additionally, this NDE approach is costly and time consuming as the bridge had to be shut down while testing takes place.

1.2 Conventional Load Rating

A rating factor is a metric used to measure how much a bridge can carry loads without it exceeding a specific factor of safety or threshold. This is important to monitor as exceeding the design load could cause failure or irreversible damage to the structure. The load rating scheme is also little different from state/county one resides in. The difference in load rating calculations creates a barrier when trying to determine a uniform and accurate load rating that works throughout the country. There are three main components in determining a rating factor (RF), which are the capacity that the element can withstand, dead load of the element, and design live load that the

element will withstand. To begin calculating an RF value, the capacity of the bridge must be found first.

For design purposes, the capacity (C) of the bridge is determined by the maximum shear and moment strength that the bridge can hold. This is done for every element on the bridge. The maximum shear and moment are determined using the bridge physical properties, such as length, material, and cross-sectional shape. The moment and shear can be calculated using section 9 of the AASHTO Standards and Specifications. Whichever value is smaller will be used to determine the capacity.

Once the maximum shear/moment is found, a condition factor and system factor can then be used to adjust the moment/shear capacity. The condition factor is based on the NBI rating given. As shown in Table 1.2.1, there is a 15% decrease from an NBI rating of a 6 to a 4. This is huge, as the inspector inspecting the bridge has a large impact on determining the capacity of the member.

Table 1.2.1 Condition Factor Chart

Structural Condition of Member	φ_c
Good or Satisfactory (NBI Item 59 >= 6)	1.00
Fair (NBI Item 59 = 5)	0.95
Poor (NBI Item 59 <= 4)	0.85

The system factor is determined based on the bridge characteristics and member connection types as well. If the bridge has more members, composite action intervenes so the strength of the bridge is increased. As shown in Table 1.2.2, three girder brides have a lower system factor then four girder brides. Also, welds typically have more uncertainty then riveted connections, due

to the welding procedure used. Because of this, welded members have a lower system factor than riveted members.

Table 1.2.2 System Factor Chart

Structural Type	φ_s
Welded Members in Two-Girder/Truss/Arch Bridges	0.85
Riveted Members in Two Girder/Truss/Arch Bridges	0.90
Multiple Eyebar Members in Truss Bridges	0.90
Three-Girder Brides with Girder Spacing 6 ft	0.85
Four-Girder Brides with Girder Spacing ≤4 ft	0.95
All Other Girder Bridges and Slab Bridges	1.00
Floorbeams with Spacing >12 ft and Noncontinuous Stringers	0.85
Redundant Stringer Subsystems between Floorbeams	1.00

Once the condition factor and system factor are found, the capacity can then be found using equation 1 (ADOT, 2011).

$$C = \emptyset_c \emptyset_s \emptyset R_n \quad (1)$$

Where C is the capacity, $\emptyset_c$ is the condition factor, $\emptyset_s$ is the system factor, and $\emptyset R_n$ is the maximum flexural/shear strength the member can withstand.

The dead load component is found by analyzing the weight of the individual structural and non-structural elements themselves. This component is split into two sections, structural component dead load and utilities (non-structural) dead load. Structural component dead loads are components that are critical in the design of the bridge, girder, slab, etc. whereas the utility dead load is the non-essential components such as the asphalt, barriers, etc. These are split up so that different modifications factors can apply, as the structural components are more critical than the utility components.

The design live load component can be calculated using the AASHTO loading conditions. Currently, HL-93 is the universal loading condition for which the bridges are typically designed for (Paulo R Rogerio, et al, 2010). This configuration is determined by the larger moment based on two separate loading conditions. The first one is two 25-kip loads placed exactly four feet apart, i.e. design tandem. The other condition is two 32-kip loads placed anywhere from 14 to 30 feet apart and an 8kip load placed 14 feet from one of the 32-kip loads, i.e. design truck. A constant .64 kip/foot load is also applied over the entire length as well, i.e. design lane load. Both loading conditions are done to replicate the actual loading conditions that different trucks present at the worst condition possible. The HL-93 loading conditions are defined in Figure 1.2.1.

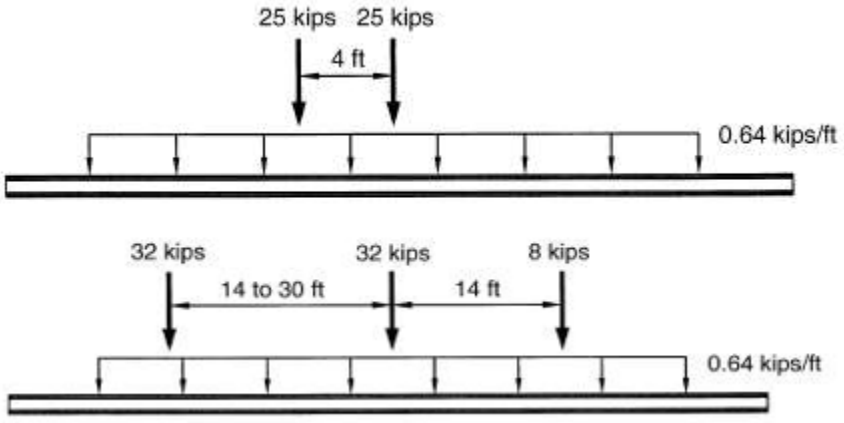

Figure 1.2.1 HL-93 Loading Conditions

The HL-93 loading condition was created in 2000's so many of these older bridges do not meet the required structural strength (ADOT,2011). This is important as many of these bridges experience frequent use and may not meet the current design requirements.

Once the capacity, dead load, and live load components are determined, a RF value can then be computed for the member using below equation (ADOT,2011).

$$RF = \frac{C - (\gamma_{DC})(DC) - (\gamma_{DW})(DW) \pm (\gamma_p)(P)}{(\gamma_{LL})(LL + IM)} \quad (2)$$

Where Table 1.2.3 describes the variables for this equation,

Table 1.2.3 Variable Description for RF Equation

RF	= Rating Factor
C	= Capacity
f'_c	= Specified compressive strength of concrete (ksi)
f'_{ci}	= Specified compressive strength of concrete at time of initial loading or prestressing (ksi)
f_R	= Allowable stress specified in the LRFD code or as stated
R_n	= Nominal member resistance (as calculated)
DC	= Dead load effect due to structural components and attachments
DW	= Dead load effect due to wearing surface and utilities
P	= Permanent loads other than dead loads
LL	= Live load effect
IM	= Dynamic load allowance
γ_{DC}	= LRFD load factor for structural components and attachments
γ_{DW}	= LRFD load factor for wearing surfaces and utilities
γ_p	= LRFD load factor for permanent loads other than dead loads = 1.0
γ_{LL}	= Evaluation live load factor
φ_c	= Condition factor
φ_S	= System factor
φ	= LRFD resistance factor
φ_w	= Hollow column reduction factor per AASHTO LRFD Bridge Design Specification, article 5.7.4.7.2

If the RF is greater than 1 than no further action is required. However, if less than one, then a new RF value must be determined with a different loading case. This is often the case for older bridges, as earlier design requirements did not have such strict load conditions. The new load case used is now the legal load, which varies based on state to state. In Texas, the maximum vehicle weight is 80 kips, the maximum tandem axle weight is 34 kips, and single axle weight is 20 kips (Texas

Department of Transportation, 2013). These loads replace the design live load and the process is repeated, with a new RF obtained. If the value is less than 1, the load must be posted on the bridge and typically, strengthening is required. If the RF value is greater than 1, then no further action is required.

A posted load is obtained when the RF is lower than 1 for the legal loads. As shown in Figure 1.2.2, the maximum weight is posted before the bridge so that the bridge does not exceed a loading condition. In theory, this is a smart procedure because it warns drivers of the capacity of the bridge. However, often drivers choose to cross these bridges anyways, as it is inconvenient to find a new route to take. Also, these signs are prone to graffiti, which makes the sign harder to see. This can cause inadvertent crashes and potential damage to the bridge.

Figure 1.2.2 Posted Load Rating of Bridge

Strengthening the bridge is typically done when the RF is less than 1 and a load rating is posted. However, strengthening a bridge requires time and money. When cities are on a strict budget, the

infrastructure is often overlooked, as evident by the D+ rating. If the RF is greater than 1, a permit load rating can be acquired. Essentially, this load scenario is for special case conditions that the bridge will rarely see. This permit load rating is not posted before the bridge. A summary of the load rating procedure is shown in Figure 1.2.3.

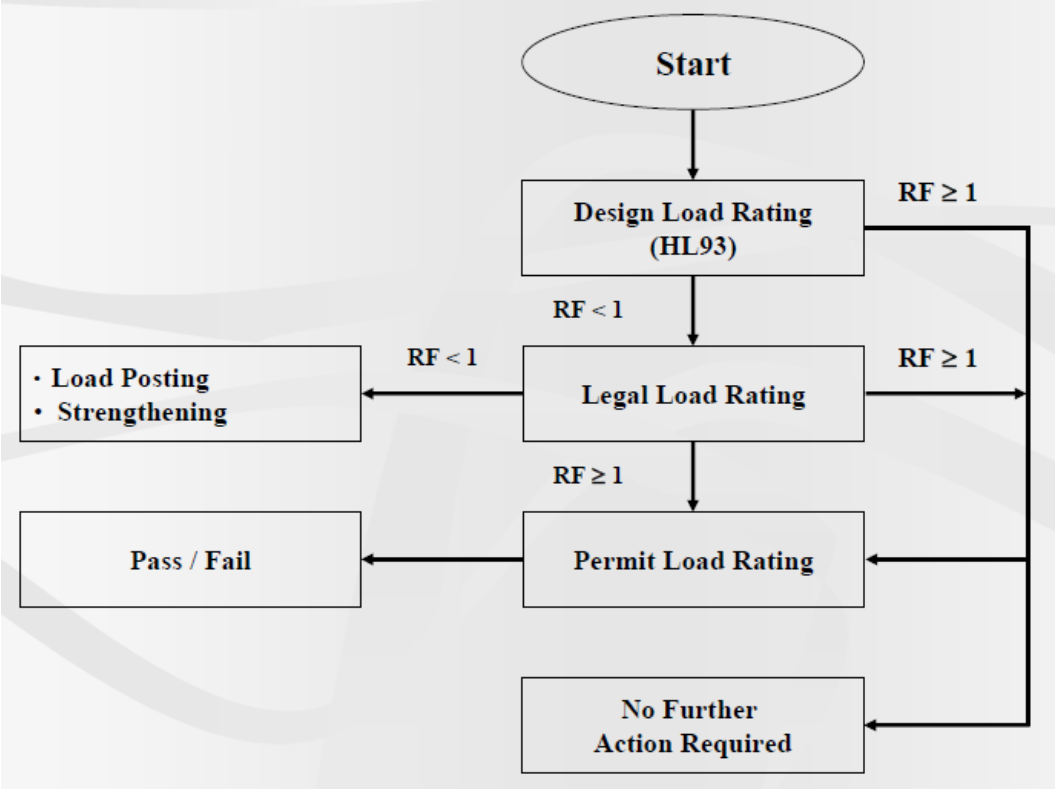

Figure 1.2.3 Summary of Load Rating Procedure

Currently, bridge load rating is done using commercial software so that updating can be performed easily. AASHTO provides two software products called AASHTO BrD and BrR at a cost. AASHTO BrD is the bridge design software. This software uses FEA to analyze the capacity of every member to make sure it is in accordance with AASHTO LRFD Specifications. AASHTO BrR is the load rating software. This software creates a load rating for every element of the bridge for every loading condition in accordance with AASHTO's Manual for Condition Evaluation of Bridges. These two software integrate within each other easily, which allows for an easy bridge design and rating

process. Another popular software choice to use when design and determining a bridge load rating is LARS Bridge. LARS Bridge is similar to the AASHTO software, except that it is one computer program instead of two. LARS Bridge can also directly access the AASHTO Bridge database directly so that the bridges analyzed can be stored for future use.

1.3 Limitations of Conventional Load Rating System

The bridge load rating process is subject to various limitations that prevent accurate values. One such limitation is that this method is subjective to human judgement. The condition factor and system factor in the rating factor equation are determined by visually inspecting the members and providing a response based on what is seen. This creates inconsistencies between the different inspectors. Furthermore, internal members cannot be visually inspected. Because of this, the members are assumed to be at full strength which could be inaccurate.

Furthermore, because the bridge inspections occur every two years in most states, the conditions of the structure are usually not properly monitored. Two years is a long time to wait in between inspection periods and potential damage can occur that was not initially accounted for. This would weaken the bridge and could potentially cause a failure if not properly monitored and managed. If inspections became more frequent, then this would generate another cost. Sending workers out to inspect the bridge is time consuming and expensive. In some cases, the bridge may even need to be shut down in order to properly inspect it. This can cause unwanted traffic delays and potential injuries towards the workers.

Another limitation of using the conventional RF approach is that the analysis is strictly based on a static approach. When determining a load rating for most cases, only the dead load, live load, and capacity of the bridge are needed. The dead load and live load are expected loading conditions but the capacity is strictly based on the geometric properties of the element, which is determined from FEA. Because of this, the dynamic properties of the bridge, such as the stiffness and damping, are not effectively considered. This can cause potential issues in seismic regions or regions with excessive flooding where a dynamic analysis is considered in the design of the bridge. The bridge can be rated for a static load but not for a dynamic loading situation. Load factors attempt to fix this by decreasing the capacity and increasing the loading for dynamic cases. However, these factors are just numbers to help account for the uncertainty of the loading situation, rather than anticipate the dynamics of the bridge under those loading conditions.

There are limitations to using the bridge load rating software as well. Because the software is so specialized, it is generally expensive. Most software's require the user to pay per the month, which can generate a large bill if the software isn't being used every day. Also, multiple licenses are usually bought at once so that multiple analyses can be run at the same time. This also generates a large cost, as multiple different licenses must to be bought as well. Furthermore, the numerical models in the software do not effectively reflect the actual bridge behavior and condition changes over time, but rather the dead load and live load effect estimations used. A bridge goes through multiple different loading conditions throughout the day which are not

accounted for in the rating factor analysis. Because of this, the actual bridge motion is not being considered when determining a rating factor.

1.4 Scope of Work

The objective of this research is to provide a cheap and effective way to estimate and monitor the actual live load carrying performance of bridges by analyzing the everyday actual loading conditions. The current rating factor process has too many limitations which makes it an ineffective way to estimate the realistic capacity of the bridge. The proposed live load performance index will be used to continuously check the live load carrying performance of the bridge regardless the 2-year inspection period.

A new way to monitor the health of a bridge is proposed using a modified rating factor. This method estimates the structural strain responses throughout the entire bridge and utilizes the strain data to create a live load performance index. This index should be higher than the design RF, as the loading applied is not nearly as high as the design load. For this approach, a model must be made where the mass, stiffness, and damping matrices can be constructed and utilized to create a state-space representation of the bridge.

Strain gages and accelerometers are placed along various locations of the bridge to accurately capture the strain and acceleration responses under various loading conditions. These loading

conditions are attributed to the everyday traffic loading that the bridge will experience, not the design loads initially used in creating the RF. Acquired sensor data in combination with a numerical model, data fusion through the Kalman filter, can be used to estimate structural responses at unknown locations throughout the whole structure. Because of this, an effective monitoring system to determine the live load carrying performance can be created using a limited number of sensors.

This research is also to be used as a template for future research endeavors. The truss tested on is a lab-scale model which is only for testing purposes. The assumptions made throughout are done so to simplify the approach. If a live load performance index can be found using this proposed method on an idealized bridge structure, then this approach can be replicated on a larger scale.

2. Hybrid Method for Live Load Carrying Performance Estimation of Bridges

A new method to continuously monitor the live load carrying performance of the bridge is proposed by combining multimeric physical monitoring and numerical modeling. This monitoring would occur in between the biennial period that the bridge load rating procedure takes place. This new approach utilizes the strain data and acceleration data gathered to estimate the strain response throughout the entire structure utilizing the Kalman filter, an advanced linear estimation algorithm. The Kalman filter approach allows the various states to be accurately estimated throughout the structure using a combination of acquired data with the finite element model under uncertainty. Basic schematic of this hybrid approach is shown in Figure 2.0.1. Each individual member of the bridge gets a LLPI based on the capacity that the member can hold versus the estimated strain.

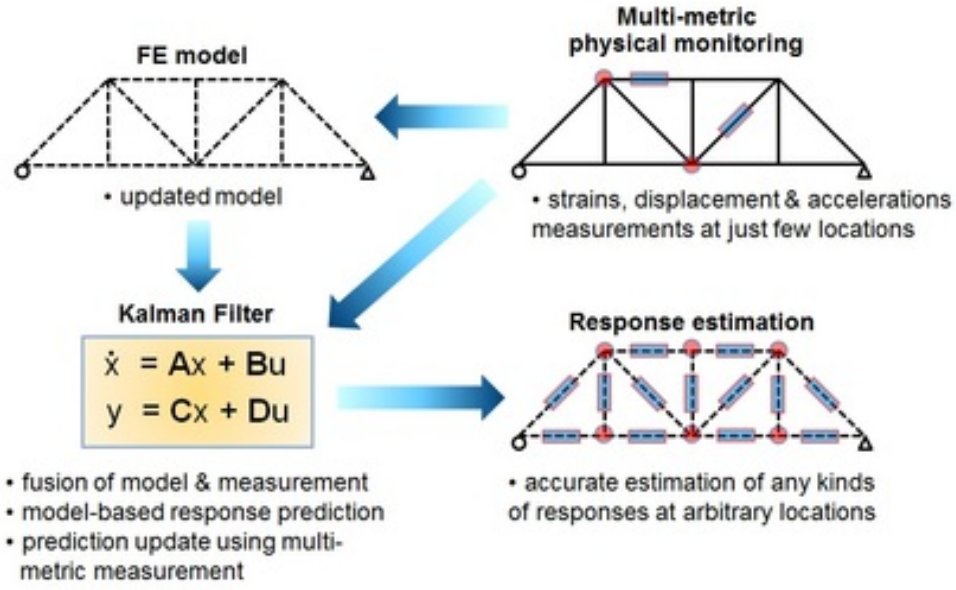

Figure 2.0.1 Hybrid Flowchart for Strain Estimation

This new proposed criterion has many advantages compared to the conventional load rating method. Because the bridge inspection procedure occurs every two years, structural damage or fatigue can occur which will not be recognized in the current load rating value. This approach allows for a live load monitoring system that would be able to track the capacity that the bridge can withstand during this 2-year period. Furthermore, the traditional "known-weight" truck approach does not need to be implemented because this procedure estimates the response of the structure due to the daily loading that the bridge experiences anytime. This eliminates the need for controlled, expensive, and full-scale strain testing utilizing a vehicle with a known weight which means the bridge does not need to get shut down.

To use this approach, an initial model is constructed using a state space representation. A state space representation is a mathematical model of the given system that is represented by the input, output, and state variables (Rowell, 2002). For this case, the system is the truss structure, the input variables are the loading conditions and the output variables are the strain and acceleration responses.

2.1 State-space formulation

For this, the dynamic system is time-invariant and linear. Because of this, we can extract a state space representation utilizing the equation of motion given in equation 3 (Craig & Kurdila ,2006).

$$m\ddot{u} + c\dot{u} + ku = p(t) \tag{3}$$

Where m is the mass matrix, c is the damping matrix, k is the stiffness matrix, u is the displacement with a function of time, $\dot{u}$ and $\ddot{u}$ are the respective derivatives, and p(t) is the force vector. From here, u and $\dot{u}$ can be turned into the state vector with respect to time as shown in equation 4.

$$x(t) = \begin{Bmatrix} u(t) \\ \dot{u}(t) \end{Bmatrix} \tag{4}$$

This equation can then be used to derive the equations of motion in different directions described by equations 5 and 6.

$$x(t) = Ax(t) + Bp(t) \tag{5}$$

And

$$y(t) = Cx(t) + Dp(t) \tag{6}$$

Where the A and B matrices are (Craig & Kurdila ,2006):

$$\mathrm{A} = \begin{bmatrix} 0 & I \\ -M^{-1}K & -M^{-1}\mathrm{C} \end{bmatrix} \; B = \begin{bmatrix} 0 \\ M^{-1} \end{bmatrix} \tag{7}$$

Furthermore, the observation matrices can be described as (Craig & Kurdila ,2006):

$$C = \begin{bmatrix} I & 0 \\ -M^{-1}K & -M^{-1}\mathrm{C} \end{bmatrix} \; D = \begin{bmatrix} 0 \\ M^{-1} \end{bmatrix} \tag{8}$$

The equation of motions described by equations 4 and 5 create a state space representation of the truss structure. Only two equations of motion are needed because the third direction receives minimal movement for the loading conditions applied.

2.2 Kalman Filter Formulation

The Kalman filter approach is a widely used estimating system that allows for a more accurate prediction by utilizing the preexisting data to estimate the next set of data. This is a widely used

application in GPS (Welch, 2006). For this experiment, a variant of the Kalman Filter was used called the augmented Kalman Filter. The augmented Kalman Filter is similar to the Kalman filter in that it utilizes a state-space model in order to estimate the state at unknown locations. However, the augmented Kalman Filter expand the state vector to accommodate the unknown excitation as a part of state variables, so that the excitation also can be estimated through the Kalman Filtering process. This is beneficial, as this setup must be repeatable for use on preexisting bridges that experience a traffic load.

As shown in Figure 2.2.1, there are 4 main steps in the augmented Kalman filter approximation approach. These are the initial state, a priori estimate, a posteriori estimate, and the final state.

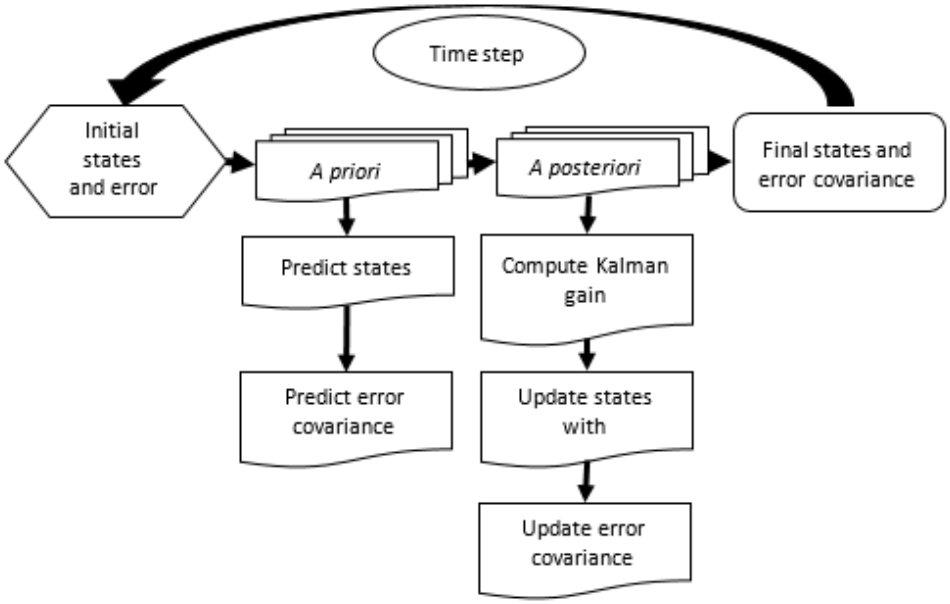

Figure 2.2.1 Kalman Filter Approach

The Initial state consists of the initial values that will be used. For this experiment, this consists of the initial displacement of the systems. These values are assumed to be zero and are given in the

state space representation. The initial values do not need to be accurate, as the Kalman filter naturally updates these based on the error derived. A general state space representation can be shown using equation 9 (Melvin, 2016).

$$\boldsymbol{y}(t) = \boldsymbol{S}_a\ddot{\boldsymbol{u}}(t) + \boldsymbol{S}_v\dot{\boldsymbol{u}}(t) + \boldsymbol{S}_d\boldsymbol{u}(t) + \boldsymbol{S}_s\boldsymbol{u}(t) \tag{9}$$

Where $\boldsymbol{S}_a$, $\boldsymbol{S}_v$, $\boldsymbol{S}_d$, and $\boldsymbol{S}_s$ are matrices to be used in the augmented Kalman filter. These matrices represent the measurements of acceleration, displacement, velocity, and strain respectively. The measured data is added to equation 8 to obtain the observation matrices shown in equation 10.

$$\boldsymbol{C} = [\,\boldsymbol{S}_s + \boldsymbol{S}_d - \boldsymbol{S}_a\boldsymbol{M}^{-1}\boldsymbol{K}\,, \boldsymbol{S}_v - \boldsymbol{S}_a\boldsymbol{M}^{-1}\overline{\boldsymbol{C}}\,], \quad \mathbf{D} = \left[\boldsymbol{S}_a\boldsymbol{M}^{-1}\boldsymbol{S}_p\right] \tag{10}$$

The *a priori* is the prediction state. This state predicts the error covariance. This is shown in equation 11 (Welch, 2006).

$$P_k = A_a P_{k-1} {A_a}^T + Q \tag{11}$$

Where P_k and P_{k-1} is the predicted error covariance an initial error covariance respectively. Q is the model covariance matrix. The covariance matrix is an assumed value that is usually found through trial and error. This was the case for this experiment, as the model covariance and strain covariance had to be optimally assumed through experimentation. A new state vector is modified to account for the unknown force used in the experiment for the augmented Kalman filter approach (Melvin, 2016).

$$\mathrm{X}_\mathrm{k}^\mathrm{a} = \begin{Bmatrix} \mathrm{X}_\mathrm{k} \\ \mathrm{p}_\mathrm{k} \end{Bmatrix} \tag{12}$$

This augmented vector is input into a state space representation to create the state space model, A, and the output vector, C (Melvin, 2016).

$$A_a = \begin{bmatrix} A & B \\ 0 & I \end{bmatrix} \tag{13}$$

$$C_a = [C \quad D] \tag{14}$$

The *a posteriori* stage follows and is the updating stage. This stage updates the values based on the Kalman gain which is derived. This is a value between 0 and 1 and it determines how much weight is given to the measured vs the estimated values. A value closer to 1 means the measurements are more accurate but the estimates are unstable whereas a value closer to 0 means that the measurements are inaccurate but there is minimal error in the estimated values. This is shown in equation 15 (Welch, 2006).

$$K_g = \frac{Estimated\ Value}{Estimated\ Value + Measured\ Value} \tag{15}$$

Which when rewritten turns into equation 16.

$$K_g = \frac{P_k {C_a}^T}{C_a P_k {C_a}^T + R} \tag{16}$$

Where R is another covariance value that is estimated initially. The Kalman gain is then used to updated the estimated measurement and the error covariance. This is shown in equation 17 and 18, respectively (Welch, 2006).

$$x_k = x_{k-1} + K_g(z_k - C_a x_k) \tag{17}$$

$$P_k = (I - K_g C_a) P_{k-1} \tag{18}$$

Where x_k and P_k are the new estimated measurement and error covariance. These new values are then repeated and inserted into the same equations which creates a time loop. A summary of the Kalman filter approach is highlighted in Figure 2.2.2.

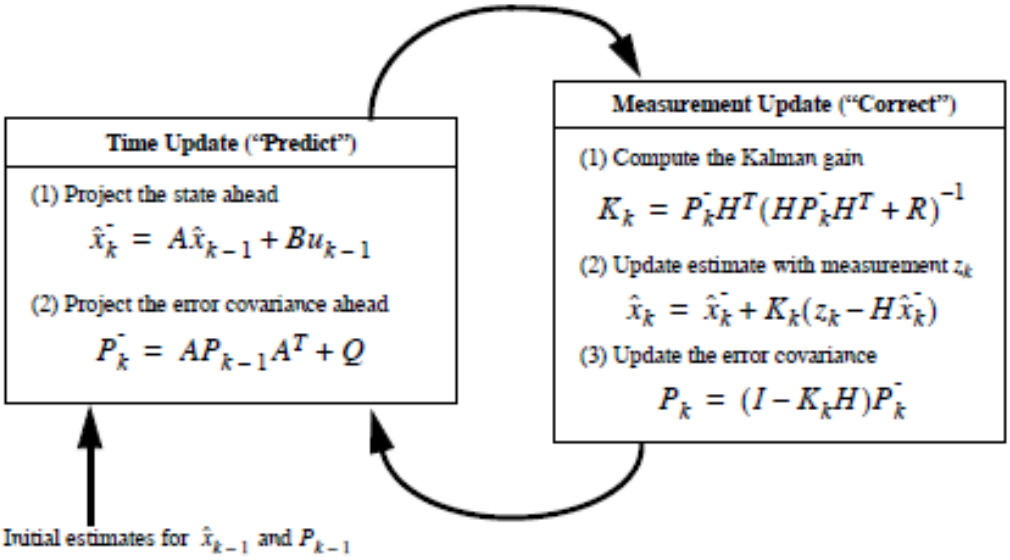

Figure 2.2.2 Summary of the Kalman Filter Approach

The Kalman Filter approach for estimation has many benefits compared to other estimation techniques. One such benefit of using this approach is that the Kalman filter can accurately predict past, present, and future states of the system, even if the modeled system isn't fully accurate. This allows for modeling error to be accepted in the initial finite element model formulation, as accurately matching a real-life structure to a numerical model has difficulties. Along with this, the Kalman Filter can accurately estimate the response while only using a limited number of sensors for the input data. This is important, as the maximum response location does not need to initially be known. This allows for more leeway when setting up the data acquisition system. Another big advantage with using the Kalman filter is that this approximation technique is more accurate than other methods such as the moving average method (Student Dave's Tutorials).

2.3 Proposed Live Load Performance Index (LLPI)

When using the Kalman Filter, strain data and acceleration data was input in order to get the displacements for every node for every degree of freedom applicable. Because the bridge analyzed for this case is a truss, equation 19 (Hibbeler, 2006) can be used to calculate the strain.

$$\varepsilon = \frac{L - L_0}{L_0} \tag{19}$$

Where ε is the strain calculated for truss members, L is the change of length determined using the Kalman filter displacements and L_0 is the initial length. L is determined using equation 20 (Hibbeler, 2006).

$$L = \sqrt{x^2 + y^2 + z^2} \tag{20}$$

Where x, y, and z are the new displacement coordinates given as outputs from using the Kalman filter for every degree of freedom analyzed.

Once the strain data was calculated, it was then used in a modified version of equation 2 to determine the LLPI as shown in equation 21.

$$LLPI = \frac{C - (\gamma_{DC})(DC) - (\gamma_{DW})(DW)}{(LL)} \tag{21}$$

The load factor variable for live load is omitted from the equation and assumed to be 1. This is because the live load effect is now a real behavior of the bridge that can be measured and estimated from the proposed hybrid method, associated uncertainties for previous live load (i.e. load factor, impact factor) can be removed. So any modification factor applied for live load would

be misleading. The live load effect (LL), axial force effect due to live load, is obtained using the strain response from the Kalman Filter approximations as shown in equation 22 (Hibbeler, 2006), particularly for truss members, which is the testbed structure for this research.

$$LL = \varepsilon * E * A \tag{22}$$

Where ε is the strain response estimated using the Kalman Filtering process, E is the modulus of elasticity, and A is the area of the element.

3. Preliminary Numerical Analysis

3.1 Truss Model

The truss model consisted of 48 nodes and 136 members. The truss is located in the Civil Engineering and Engineering Mechanics building at the University of Arizona in room CE110. The location and simplicity of this structure make it an ideal bridge for initial testing on. The members have a hollow, circular cross-sectional area and are made from 1018 steel. The nuts and bolts used to connect the members were also made from 1018 steel. The node is a solid piece of 1018 steel with tapped holes to allow the members to connect. These parts were all made available off the shelf for easy access and replacement if needed.

Figure 3.1.1 Truss Model

Torsional problems were occurring due to the lack of diagonal members between the bays. Nylon rope was added as diagonal members to eliminate the torsional issues. There were 20 cable elements that were added to the bridge, which increased the total number of elements to 156.

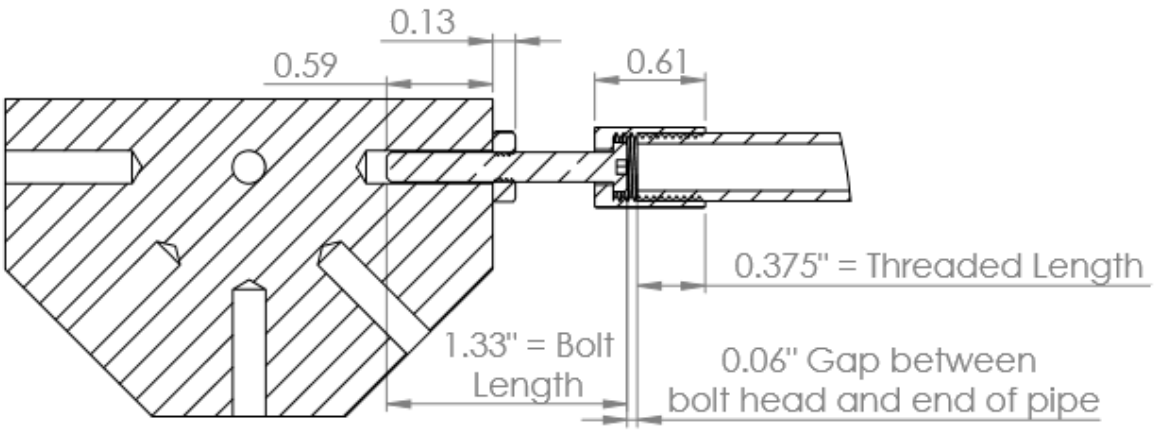

Figure 3.1.2 Node-Element Connection

The joints of the members have a 2-inch offset that is caused by the nut and node interaction. This was later modeled in both the MATLAB and SAP2000. The member and cable properties were also determined using the MATWEB, an online database for material information.

Table 3.1.1 Initial Member Properties

Beam Properties			
Modulus of Elasticity (E)	=	29,700,000	psi
Cross-sectional Area (A)	=	0.0578	in^2
Density (P)	=	0.284	psi
Cable Properties			
Modulus of Elasticity (E)	=	435,115	psi
Cross-sectional Area (A)	=	0.0767	in^2

The truss consists of 13 bays long, 1 bay high, and 1 bay wide. The truss is approximately 180” in the x-direction, 24” in the y-direction, and 15” in the z-direction. These dimensions are measured from the center of the nodes. The end connections are pinned on one end (nodes 25 and 26), and a roller connection on the other end (nodes 1 and 2).

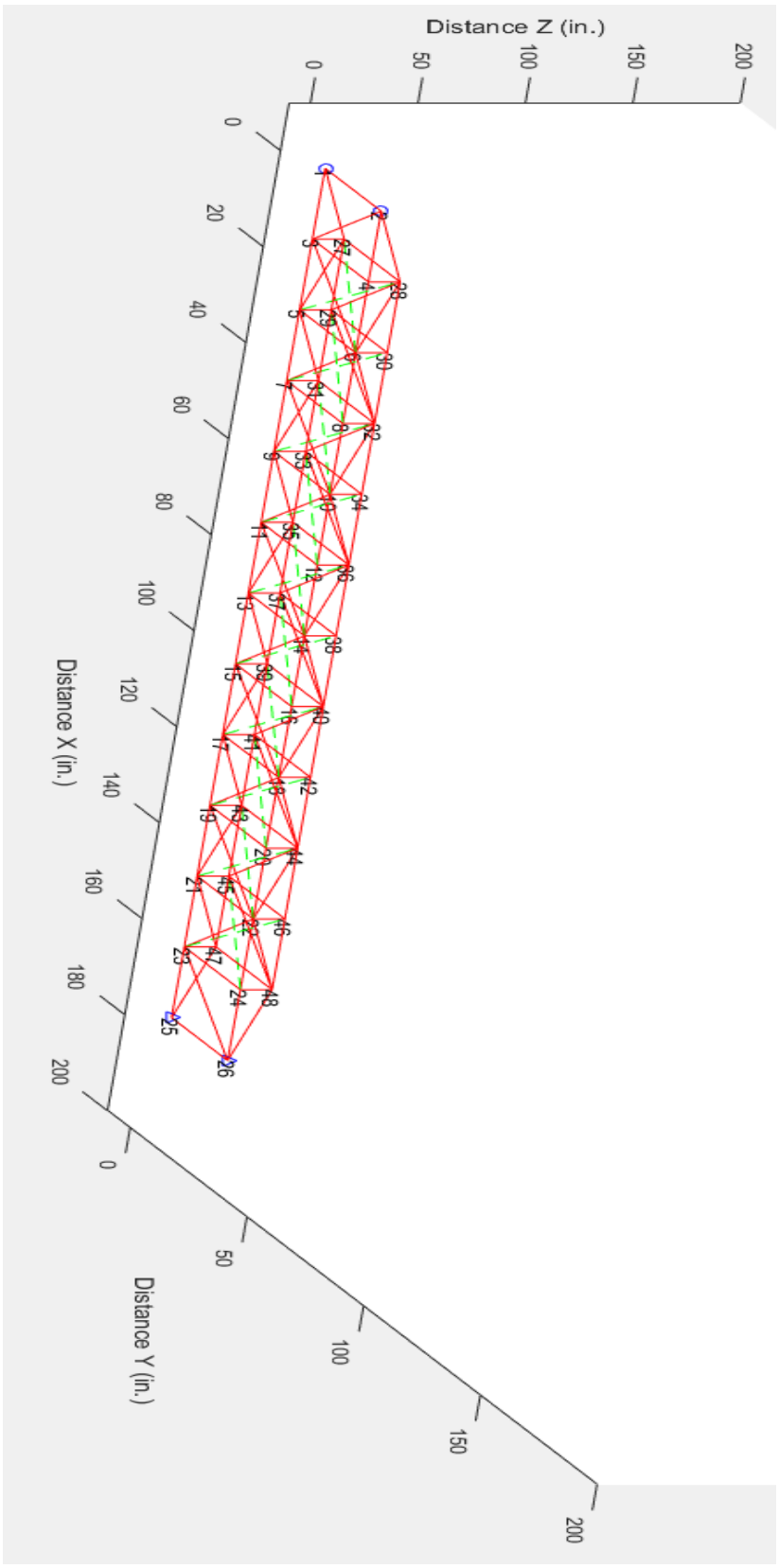

Figure 3.1.3 3D view of the Truss

3.2 Structural Analysis Using SAP2000

A finite element model for the truss structure was first created in SAP2000. SAP2000 is a finite element software that is widely used for structural analysis and design of various structures. The same properties and parameters that reflect the actual truss bridge were used in when creating this. Nodes 1 and 2 are roller connections with movement only allowed in the x-direction whereas nodes 25 and 26 are pinned connections with no movement allowed but rotation along the y-axis is allowed.

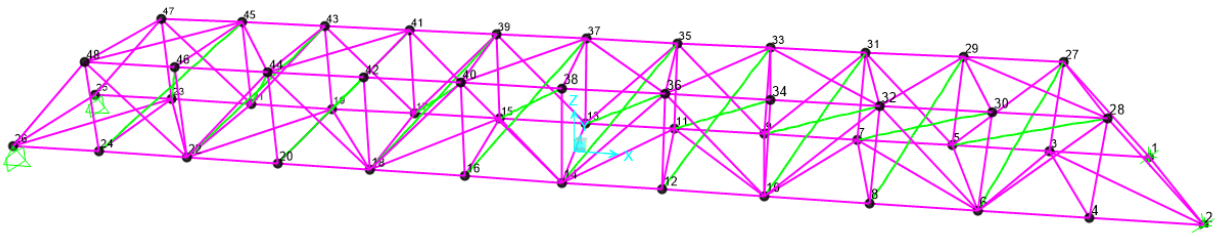

Figure 3.2.1 SAP2000 Model

The SAP2000 model was created and used as a reference. This was done as to verify the accuracy of the test results throughout the experiments. Furthermore, the SAP2000 model was also used to determine the location of high strain values when a unit point load is applied. The elements that generated a large amount of strain had strain gages placed on them. For the SAP2000 model to be accurate, the dynamic properties of the model and the truss must accurately match.

SAP2000's internal modal analysis program automatically generates the mode shapes and natural frequencies for the structure. Two different methods can be used to obtain this, Eigenvector analysis and Ritz-vector analysis. As shown in equation 23, the eigenvector analysis determines

the natural, undamped mode shapes and frequencies associated with the parameters of the structure (Craig & Kurdila, 2006). Eigenvector analysis is more commonly used due to the simplicity and for not needing an excitation (SAP2000: integrated software for structural analysis and design, 2006).

$$[K - \Omega^2 \mathrm{M}]\emptyset = 0 \tag{23}$$

Where K is the stiffness matrix, Ω^2 is the diagonal eigenvalue matrix, M is the mass matrix, and Ø is the corresponding eigenvector matrix. Ritz-vector analysis finds the modes and frequencies that are excited by a force. Ritz-vector analysis is generally more precise; however, computation time and effort is often longer. The eigenvector approached was used to determine the mode shapes and natural frequencies of the SAP2000 model.

Table 3.2.1 Natural Frequency's using SAP2000's Eigenvector Analysis

Mode	Natural Frequency (Hz)
1	10.38
2	14.08
3	30.28
4	31.58
5	45.97
6	55.94

Only the first 6 mode shapes were analyzed because the higher frequency mode shapes are generally harder to determine through experimental testing. In addition to finding the natural frequency's, the mode shapes were also analyzed. Because the sensors will be placed in the z-direction, the non-torsional modes are easier to capture. For this, modes 2 and 6 were the non-torsional modes analyzed.

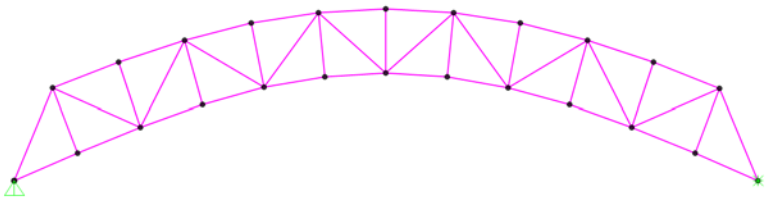

Figure 3.2.2 Mode Shape 2 using SAP2000

Mode shape 2 shows a uniform displacement across the whole structure. The middle of the truss shows the largest displacement, whereas the ends show minimal displacement. The next mode shape analyzed is mode shape 6. This mode is shaped looks like a wave with the quarter points being the largest displacement whereas the middle and ends have minimal displacement.

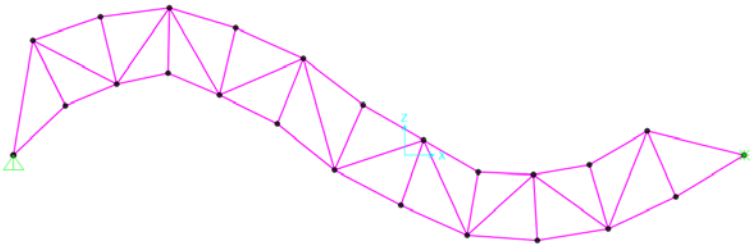

Figure 3.2.3 Mode Shape 6 using SAP2000

After determining the dynamic properties, the SAP2000 model was used to validate the maximum strain location. For doing this, a unit point load was applied on node 44. This node was chosen as it is a quarter point along the truss structure so large strain values can be determined for mode shapes 2 and 6.

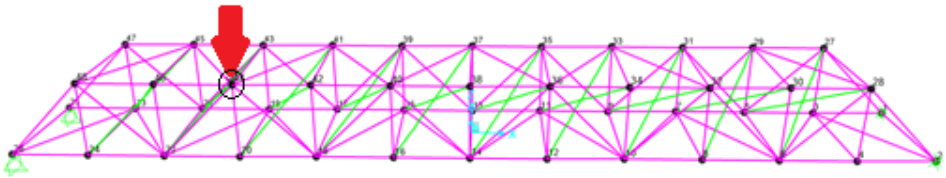

Figure 3.2.4 Point Load Location

In order to determine the strain, the axial force was first found at every member. This was determined using SAP2000's internal analysis program. The axial stress directly correlates to the member's strain through basic mechanics of solids as shown in equations 24 and 25 (Desai, 2001).

$$\sigma = \frac{P}{A} \tag{24}$$

Where P is the axial force, A is the area, and σ is the stress. Because the area of each member is the same, the stress is directly related to the force. Thus, the strain is also in a direct relationship (Desai, 2001).

$$\varepsilon = \sigma / E \tag{25}$$

Where E is the modulus of elasticity and ε is the calculated strain. Since all members are made from the same material, the modulus of elasticity is the same for every element. The strain is then proportional to the stress which is proportional to the axial force.

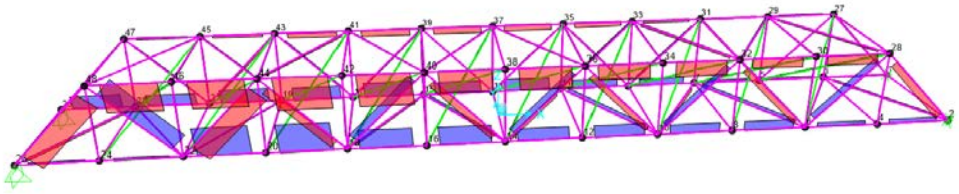

Figure 3.2.5 Axial Force Distribution Across Truss

The elements closest to the unit point load receive the largest axial force whereas the elements farthest away receive the least axial force. Furthermore, the elements on the side of the truss where the unit point load is applied receive more axial force then elements on the other side, as depicted in Figure 3.2.5. Because of this, the strain gages were placed on the side of the truss where the loading occurs and on members that experience a large axial force. After creating the SAP2000 model, the dynamic properties of the truss were found using a data acquisition system.

4. System Identification of Truss Structure

4.1 Experimental Setup

A 24-bit data acquisition system (DAQ), NI CompaqDAQ-9178 with NI9234 & NI9235 modules, was used to obtain the structural response data at given locations on the structure. This information was then used to determine the modal properties of the truss. Multimeric responses, i.e. strain and acceleration, are measured. The strain gauges were placed in the middle on the top of the elements (Figure 4.1.3) whereas the accelerometers were placed on the bottom of the bottom nodes (Figure 4.1.1). The strain data and acceleration data obtained was used to estimate the strain responses throughout the entire structure using the augmented Kalman Filter. The acceleration data was also used to determine the modal properties of the truss. This was done by peak picking method using the cross power spectral density (CPSD) of the acceleration data.

Two different loading conditions were used to estimate the strain and obtain the dynamic properties. The first loading condition was the “Impact Force” test. A singular node was hit with a hammer. The node that got chosen was node number 44, which was chosen because it was the node that the unit point load was placed on in the SAP2000 model. The node was hit with a hammer to reduce the inherit damping that could be caused by using a softer, more malleable, material. The sample size for the impact force test was approximately 300 seconds. This was done so that an ample amount of time was recorded to find the mode shapes and the natural frequencies with less noise.

The second loading condition that was done was the “Random Excitation” test. Node 44 was randomly hit with minimal force but at random intervals. This was not done with a hammer, but rather with the knuckles, as a hammer would apply too much force. The sample size for this test was approximately 300 seconds. This was deemed enough time to accurately predict the strain through the Kalman filter approach. Each test that was ran using a sampling rate of 2000 Hz.

Both tests were done for demonstration purpose rather than simulating the real-life bridge conditions. But the impact load could actually be anything ranging from an accidental collision from a car to a large wave caused by excessive flooding. The random excitation test may be similar to the traffic loading in some sense on a bridge, as it is random with a slight force applied. As long as any realistic loading data is available, it can be applied to the structure using a shaker available in the Smart Structure System Lab at the University of Arizona.

Total 19 accelerometers were used for the tests. All the accelerometers were placed so that they would measure the acceleration in the z-direction. Because of this, only the mode shapes that displace in the z-direction will be analyzed.

Figure 4.1.1 Individual Accelerometer Location

Due to the limited number of sensors available, sensors were not able to be placed on all locations. Because of this, only in the nodes where the accelerometers were placed, the mode shapes can be captured.

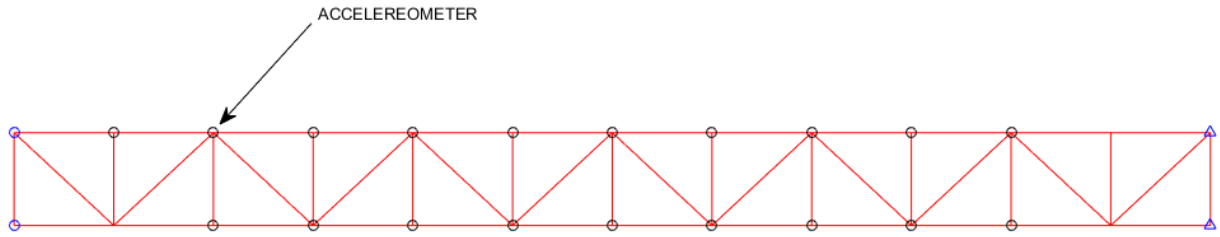

Figure 4.1.2 Accelerometer Locations on the Bottom Nodes of the Truss

Three strain gages were used to acquire dynamic strain responses. The truss element surface were slightly grinded and cleaned so that when the strain gages were installed, the surface would be flat and smooth to eliminate potential error. Figure 4.1.3 shows the installation of a single strain gage on a truss element.

Figure 4.1.3 Individual Strain Gage Location

The strain gages were placed on the elements that would experience a large strain in the SAP2000 modeling when a unit load was applied. The strain gages were spaced out as to capture as much of the bridge action as possible. One strain gage was placed on the element that experienced the largest strain. This element is connecting to node 44, the node where the force was applied. The location of these gages is shown in Figure 4.1.4

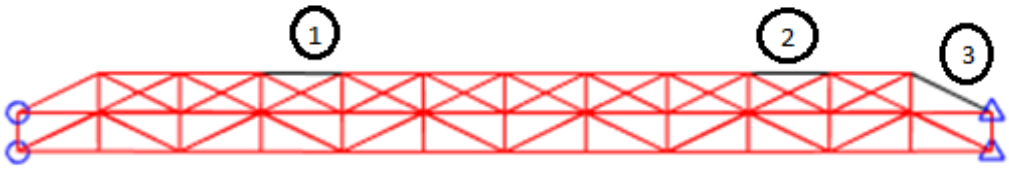

Figure 4.1.4 Strain Gage Locations across the Whole Truss

4.2 Strain and Acceleration Response Measurement

The strain and accelerometer data was acquired for the given time interval. The first set of strain data is for the impact force test, as shown in Figure 4.2.1. The peaks of the strain gage data are when the hammer was hitting the node. This is easy to see, as a large force was applied. This causes a large strain initially, but it eventually settles to rest as no yielding takes place. The second and third graphs appear accurate, as there is minima noise with large, noticeable peaks. However, the first graph shows drifting in strain over time, with substantial low-frequency noise. This could be due to poor sensor installment, as the strain gage was more than likely moving over time. Because of this, this sensor was not used in any of the post-processing results.

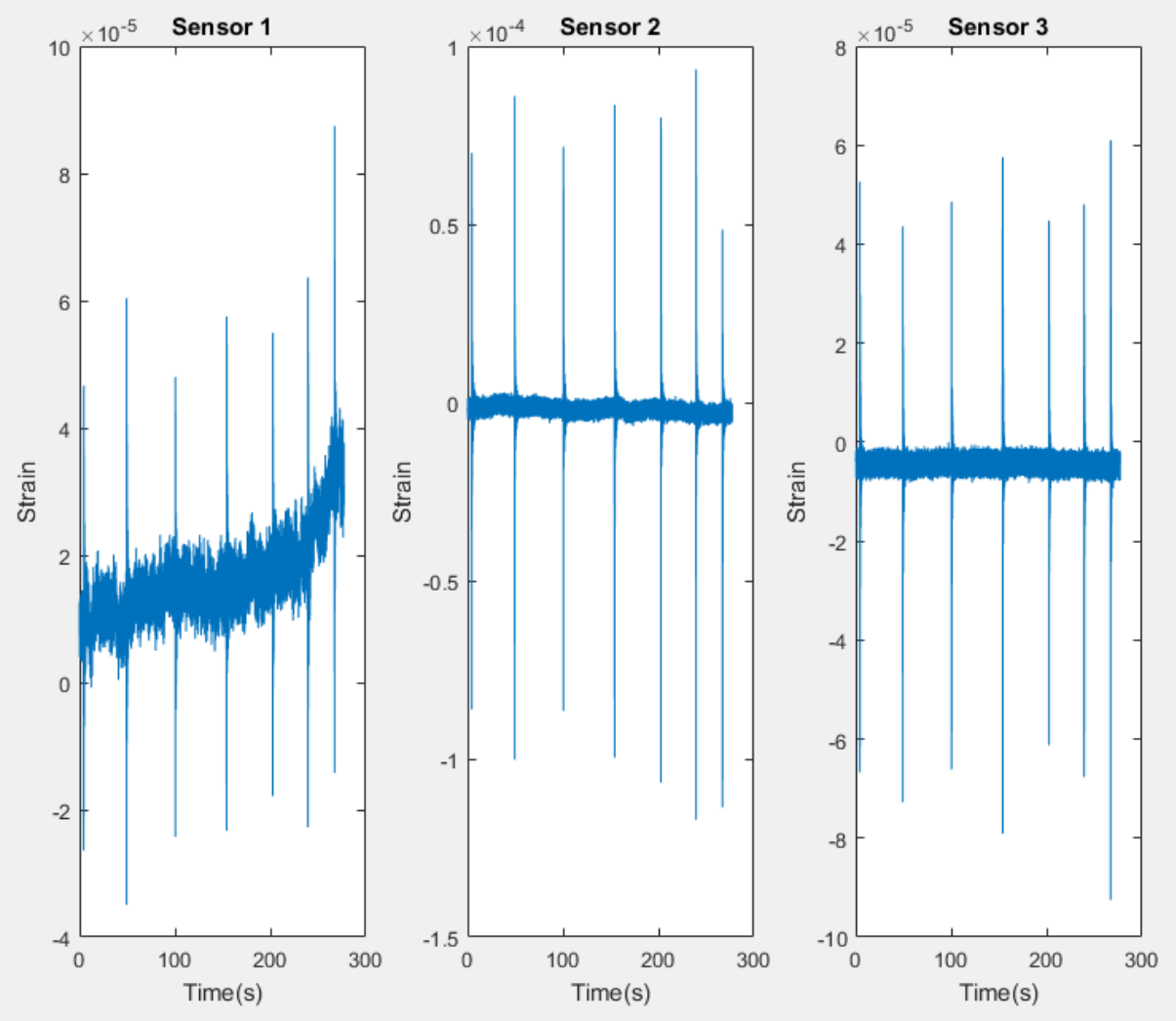

Figure 4.2.1 Strain Measurement for the Impact Force test

After analyzing the peaks of each graph, the maximum strain over the five-minute interval was determined for the impact force test, because the lowest (i.e. critical) LLPI value is determined using the maximum response. This is shown in Table 4.2.1. These strain values are compared to the estimated strain values that the Kalman filter approach predicts later.

Table 4.2.1 Maximum Strain Measured for the Impact Force test

Strain Gage Number	Maximum Strain Measured
2	1.17E-04
3	9.25E-05

The second set of strain data is for the random excitation test. These strain values appeared just as accurate as the impact force test data. The second and third strain gages appear to show a linear trend as time progresses, with the peaks being caused by the random excitations of the node. The first strain gage appears to shift up and down as time progresses. Because of this, this strain gage was not used in any of the post-processing analysis as well.

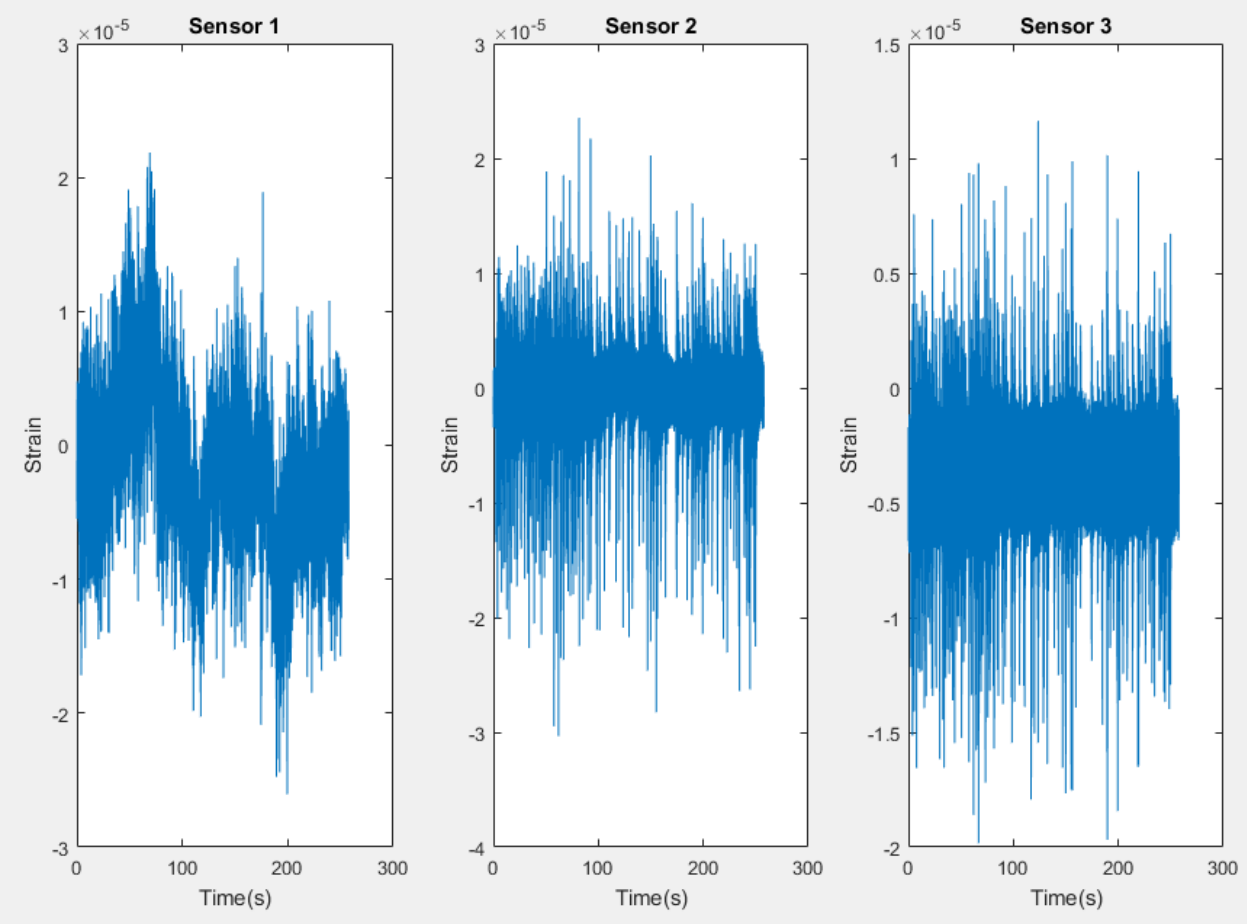

Figure 4.2.2 Strain Measurement for the Random Excitation Test

The maximum strain was then measured and obtained from the three different strain gages. Because the force applied during the Random Excitation test is smaller than the force applied during the Impact Force test, the maximum strain values found are smaller. These strain values are used as comparisons for the strain values estimated using the Kalman Filter.

Table 4.2.2 Maximum Strain Measured for the Random Excitation Test

Strain Gage Number	Maximum Strain Measured
2	3.03E-05
3	1.98E-05

The acceleration data was also found for all 19 accelerometers. The acceleration data for the impact force test shows multiple peaks for the time sample. Theses peaks are where the hammer was hit on node 44. As opposed to the strain data, all acceleration data looks accurate. The acceleration data for the random excitation test looks accurate as well. The acceleration data obtained from accelerometer 17 shows a large amount of acceleration occurring. This is the accelerometer under the node that is closest to the location where the force was applied. For both tests, the acceleration data ranges from -5 to 5 g's. Figures 4.2.3 and 4.2.4 show the acceleration data obtained from the Impact Force test and the Random Excitation test, respectively.

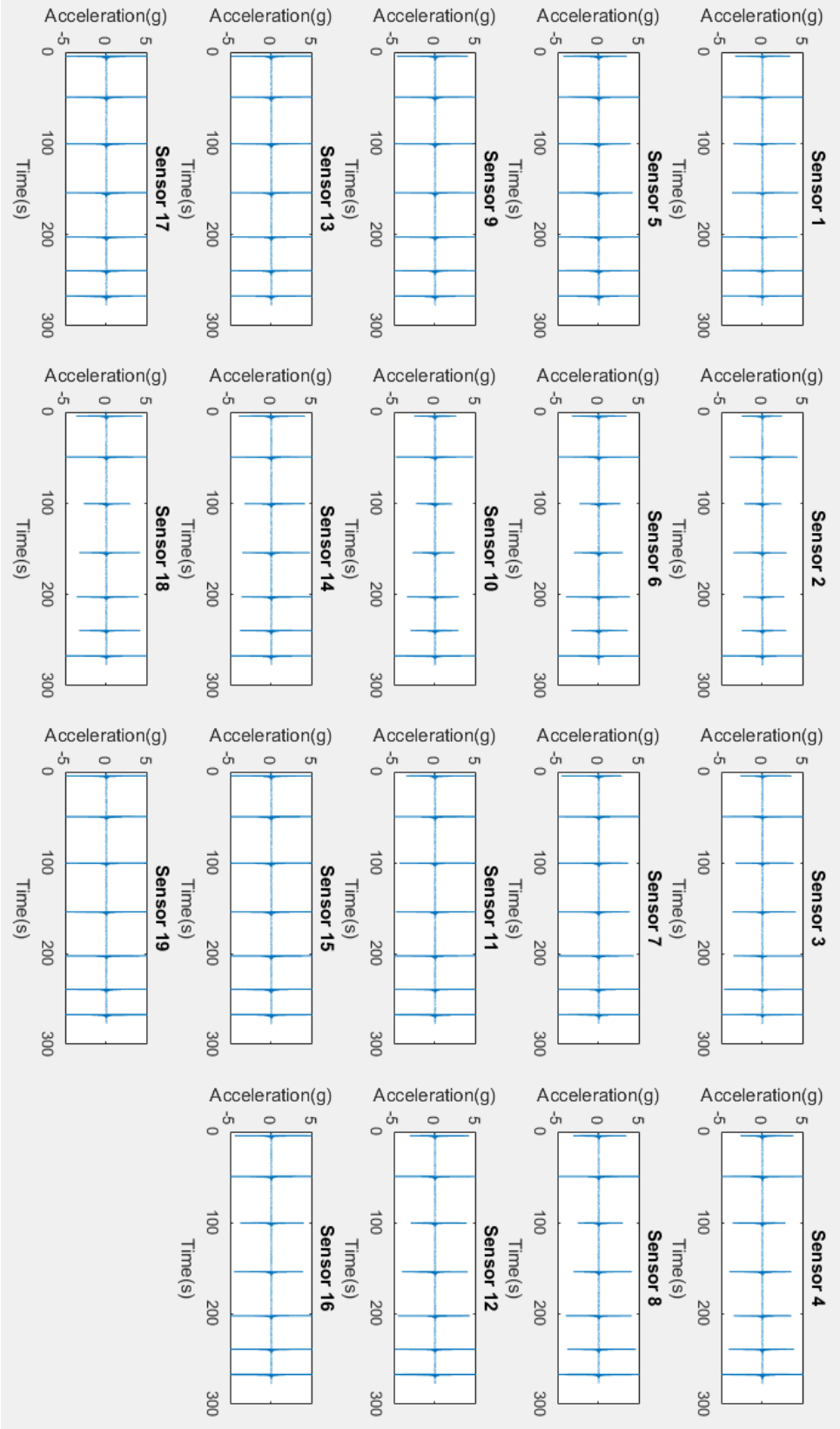

Figure 4.2.3 Acceleration Measurement for Impact Force Test

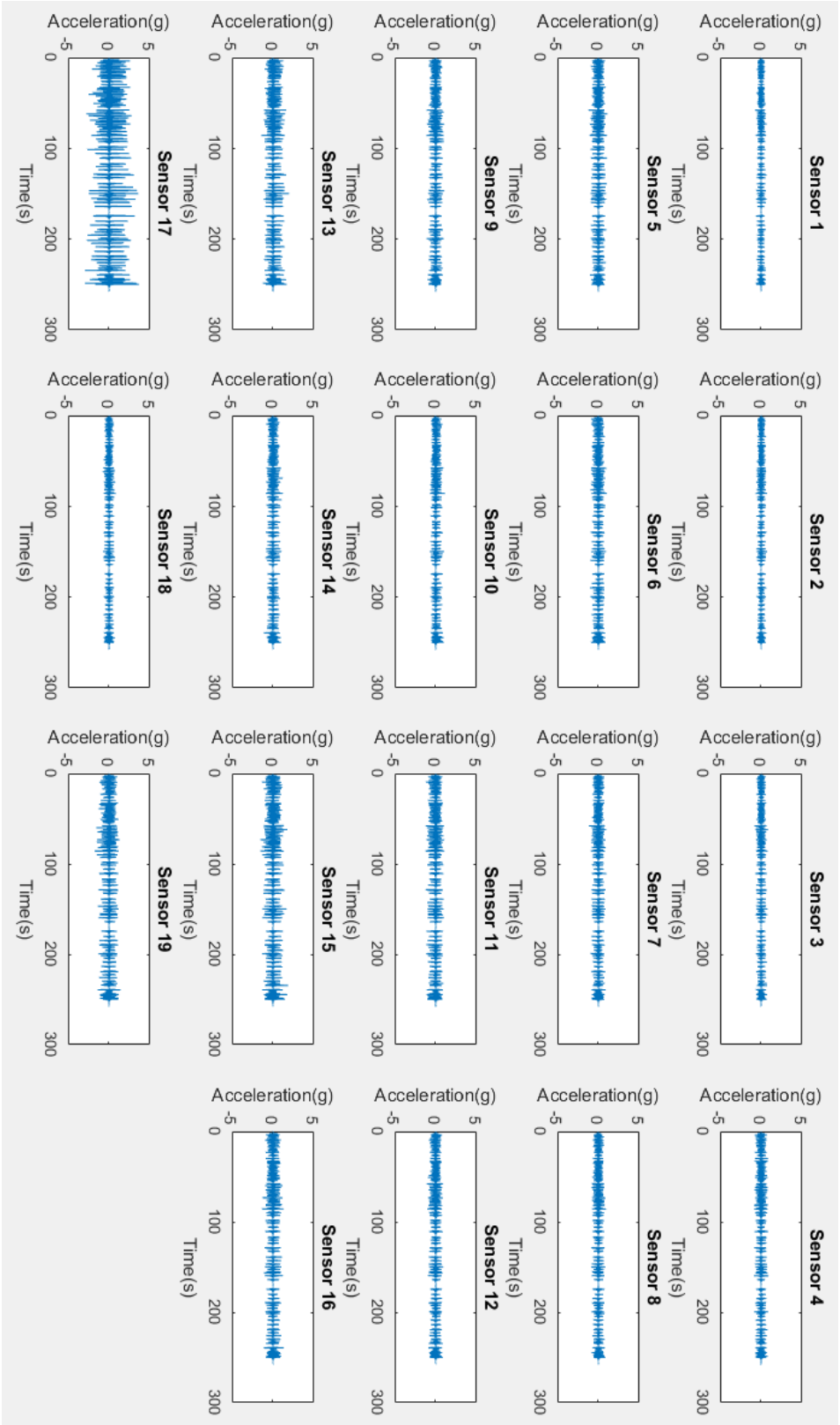

Figure 4.2.4 Acceleration Measurements for the Random Excitation Test

The acceleration data obtained from the random excitation test was used for the system identification. This set of data was used versus the impact force test acceleration data because the acceleration data obtained from the random excitation test is more accurate when using the power spectral density analysis. This is because the truss is being dynamically excited more under the random excitation test versus the impact force test.

4.3 Modal Identification

The acceleration data obtained was used to determine the modal properties of the truss structure. Power spectral density (PSD) was used to determine the energy distribution of the acceleration data over the measured frequency bandwidth, which in turn was used to determine the natural frequencies, phase angles, and mode shapes using the peak-picking method. This method was done using Welch's averaged, modified periodogram method shown in equation 26 (Craig & Kurdila, 2006).

$$G_{AB} = A(f)B(f)^* \tag{26}$$

Where G_{AB} is the cross-power spectrum and *A(f)* is the Fourier transform measurement of one acceleration sensor and *B(f)** is the complex conjugate of the Fourier transform of another acceleration sensor measurement in domain *A(t)* and *B(t)*, respectively. If the *A(t)* and *B(t)* are the same data, then the G_{AB} is the auto-power spectrum. Hanning window was used to reduce spectral leakage in the Fourier Transform process. This window function is given by equation 24 (National Instrument, 2016).

$$w(n) = \frac{1}{2}\left(1 - \cos\left(\frac{2\pi n}{N-1}\right)\right) \tag{27}$$

Where N is the total number of samples and n is a real number in the domain 0 to N-1. The natural frequencies are then determined using peak picking method. This method states that the peaks of the power spectral density can get excited easier when power is applied (Craig, 2006). This means that the amplitudes of the power spectral peaks of different sensor measurements at the given frequency can determine relative movement of the nodes where the sensor data are measured.

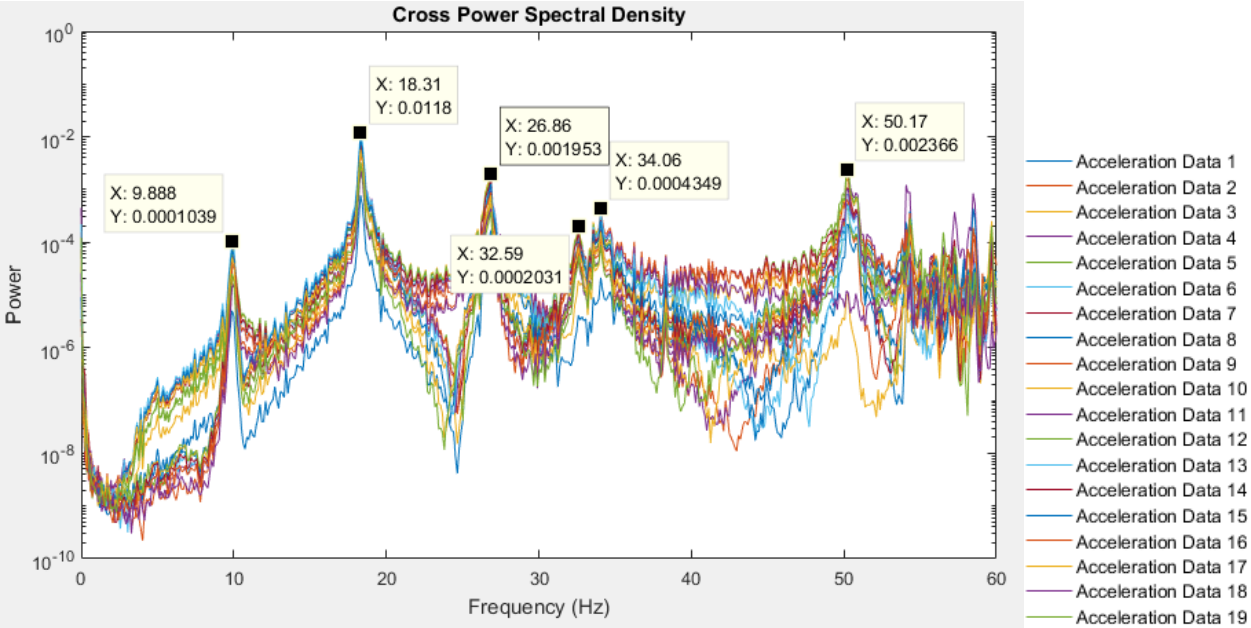

Figure 4.3.1 Cross-Power Spectral Densities of Acceleration Measurements for the Random Excitation Test

The plot in Figure 4.3.1 shows 6 distinct peaks with frequency values ranging from 0 to roughly 50 Hz. In this study, the first 6 natural frequencies are only used as higher frequency peaks have more noise involved; which would be sufficient because most dynamic energy is concentrated on low frequency natural modes.

The power values at each peak were analyzed to determine the prominence of each mode. A larger value indicates that the mode shape is more prominent than a smaller value. The second and sixth natural frequency peaks have the largest values at values .0118 and .00236, respectively. These are both the non-torsional modes as analyzed in SAP2000. Because the sensors are only placed in the z-direction, these modes are expected to receive the most power when performing PSD. Peak picking method provides the natural frequency values for the structure. These are the values where the peaks occur. These values are shown in Table 4.3.1.

Table 4.3.1 Natural Frequency Values for Truss Structure

Mode	Natural Frequency (Hz)
1	9.88
2	18.31
3	26.73
4	32.84
5	34.55
6	50.29

The natural frequency values obtained from sensor measurement were then compared with the values obtained using the SAP2000 model. There is sizeable error between the natural frequency values from the SAP2000 model and the actual truss bridge behavior. This error may stem from the fact that the truss bridge was assembled by hand with different torque values at each node locations and may have different level of geometric stiffness in each member.

Table 4.3.2 Natural Frequency Comparison Between the Truss and SAP2000 Model

Mode	SAP 2000 Natural Frequency (Hz)	Truss Natural Frequencys (Hz)	Error (%)
1	10.38	9.88	5.06
2	14.08	18.31	-23.10
3	30.28	26.73	13.28
4	31.58	32.84	-3.84
5	45.97	34.55	33.05
6	55.94	50.29	11.23

Where the error is calculated using equation 25 (Hibbeler, 2006).

$$error = \frac{Approx. - Exact}{Exact} * 100 \tag{28}$$

The mode shapes were then found by comparing the relative amplitudes of the PSD peaks between different node measurements and phase differences at the given natural frequencies. Modes 2 and 6 are the non-torsional mode whereas modes 1, 3, 4, and 5 all experienced some torsion. This closely matches the results obtained from SAP2000. Mode 2 is the first bending mode shape that occurs and the maximum deflection occurs in the middle. The mode shape matches mode shape 2 obtained from the SAP2000 analysis.

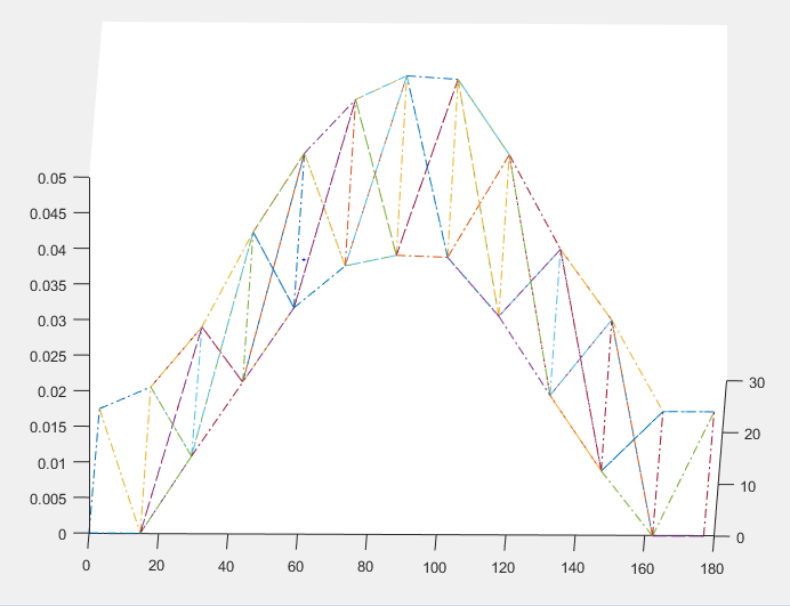

Figure 4.3.3 1st Bending Mode Shape Using Peak Picking Method

The sixth mode shape is the second bending mode shape. There are two distinct peaks, one positive and one negative along the span. The middle and ends of the truss also experiences minimal displacement. This mode shape matches mode shape #6 using the SAP2000 model.

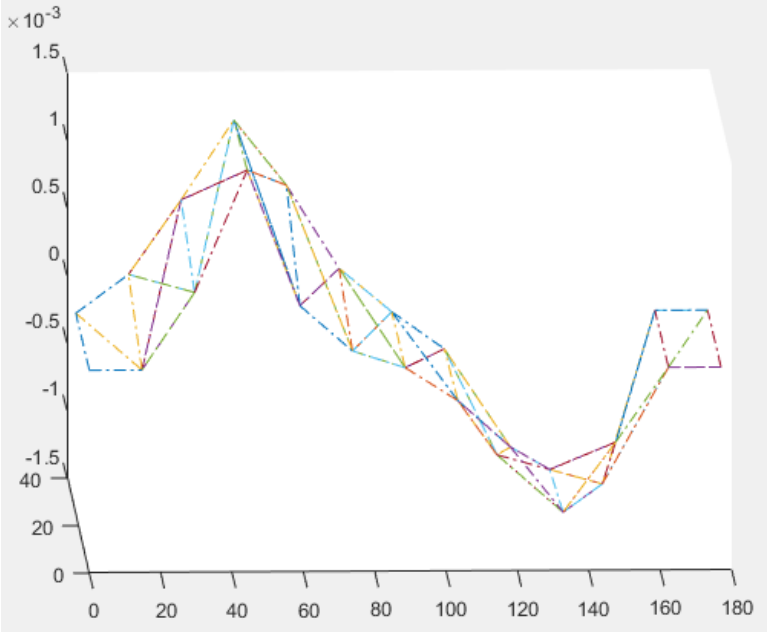

Figure 4.3.4 2nd Bending Mode Shape Using Peak Picking Method

The mode shapes and natural frequencies found for the truss are close representations to the ones found in SAP2000. However, there is some error between the truss structure and the SAP2000 model. This is evident as the mode shapes for the truss found using CPSD are not smooth whereas the ones found in SAP2000 are smooth; which may be attributed to the fact that spectral resolution may not be sufficient by using relatively higher sampling rate (i.e. 2000Hz) for 0~50 Hz dynamic structure and each sensors have somewhat different sensitivities. However, the augmented Kalman filter approach that utilizes experimental data, along with numerical models, to estimate response, can accommodate uncertainties in numerical model and sensor measurement, so such errors may be in acceptable range for the Kalman Filtering process.

5. Finite Element Model of Truss Structure Using MATLAB

A finite element model was made using MATLAB so can be interfaced with the Kalman Filter algorithm to estimate the strain across the whole structure. The mass and stiffness matrices were then obtained so that a state space representation could be made. Model updating was then performed in order to accurately describe the truss characteristics.

5.1 Finite Element Model Using MATLAB

Along with generating a SAP2000 model, a numerical model was made in MATLAB. The SAP2000 model provided a reference when the MATLAB model was being created. The MATLAB model has the same physical properties as the truss analyzed.

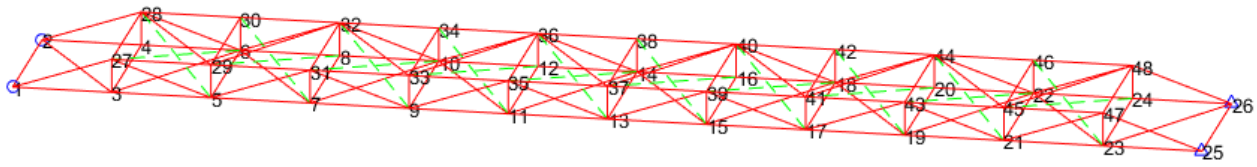

Figure 5.1.1 MATLAB Model

For a truss structure, the assumed DOF were x, y and z translation only. This differentiates itself from a frame, which has all 6 DOF applied to it. From this, the single element mass matrix was constructed. The mass of the cable elements is minimal, so it was ignored in the analysis.

Two different mass matrix formulations were considered for determining the global mass matrix, direct mass lumping and consistent mass lumping. Direct mass lumping consists of assuming the

total mass of the individual member and dividing it equally between the two end nodes as describe by equation 29 (Colorado, 2012).

$$m = \frac{1}{2}\rho Al\begin{bmatrix}1 & 0 & 0 & 0 & 0 & 0\\ 0 & 1 & 0 & 0 & 0 & 0\\ 0 & 0 & 1 & 0 & 0 & 0\\ 0 & 0 & 0 & 1 & 0 & 0\\ 0 & 0 & 0 & 0 & 1 & 0\\ 0 & 0 & 0 & 0 & 0 & 1\end{bmatrix} + m_{node} \tag{29}$$

Where ρ, A, l is the density, area, and length, respectively. m_{node} is the mass of the node and was measured out to be 1.41 lb. This method is generally considered simpler and allows for quicker processing times due to that fact that a diagonal matrix is created. The other method used for determining the global mass matrix is the consistent mass matrix method. The consistent mass matrix does not result in a diagonal matrix, which further creates computation time. This method is usually more accurate because it derived from consistent principles, meaning certain nodes carry more mass then other nodes as shown in equation 30 (Gavin, 2014).

$$m = \frac{\rho Al}{6}\begin{bmatrix} 2c_xc_x & 2c_xc_y & 2c_xc_z & c_xc_x & c_xc_y & c_xc_z\\ 2c_yc_x & 2c_yc_y & 2c_yc_z & c_yc_x & c_yc_y & c_yc_z\\ 2c_zc_x & 2c_zc_y & 2c_zc_z & c_zc_x & c_zc_y & c_zc_z\\ c_xc_x & c_xc_y & c_xc_z & 2c_xc_x & 2c_xc_y & 2c_xc_z\\ c_yc_x & c_yc_y & c_yc_z & 2c_yc_x & 2c_yc_y & 2c_yc_z\\ c_zc_x & c_zc_y & c_zc_z & 2c_zc_x & 2c_zc_y & 2c_zc_z \end{bmatrix} + m_{node} \tag{30}$$

Where ρ, A, and l is the density, area and length, respectively. c_x , c_y , and c_z is the directional cosines with respect to the three-coordinate axis. The direct mass lumping was ultimately used to decrease computation time with fairly accurate results.

After the individual mass matrices were obtained, a global matrix was obtained by combining all the individual mass matrices with respect to the DOF allocated to each member as shown in equation 31 (Desai, 2001).

$$M = \begin{bmatrix} m_1 & \cdots & 0 \\ \vdots & \ddots & \vdots \\ 0 & \cdots & m_n \end{bmatrix} \tag{31}$$

This creates a global, diagonal matrix, which was used to obtain the natural frequencies of the truss.

The individual stiffness matrix was calculated using a finite element approach also. The approach that was used is the direct stiffness matrix method. This method relates the members stiffness directly with the force and displacement applied. The benefits of using this method is that the computation times are quicker than using other methods, as the matrix formulation is quite simple. This was constructed utilizing equation 32 (Gavin, 2014).

$$k = \frac{AE}{l}\begin{bmatrix} c_x c_x & c_x c_y & c_x c_z & -c_x c_x & -c_x c_y & -c_x c_z \\ c_y c_x & c_y c_y & c_y c_z & -c_y c_x & -c_y c_y & -c_y c_z \\ c_z c_x & c_z c_y & c_z c_z & -c_z c_x & -c_z c_y & -c_z c_z \\ -c_x c_x & -c_x c_y & -c_x c_z & c_x c_x & c_x c_y & c_x c_z \\ -c_y c_x & -c_y c_y & -c_y c_z & c_y c_x & c_y c_y & c_y c_z \\ -c_z c_x & -c_z c_y & -c_z c_z & c_z c_x & c_z c_y & c_z c_z \end{bmatrix} \tag{32}$$

Where E is the modulus of elasticity for the member. Once the individual stiffness matrix was constructed, the global stiffness matrix was then constructed utilizing the same method as the global mass matrix. However, the stiffness matrix is not diagonal. The matrix is constructed utilizing the i an j DOF for the elements as shown in equation 33 (Desai, 2001).

$$K = \begin{bmatrix} k_{1,1} & \cdots & k_{1,j} \\ \vdots & \ddots & \vdots \\ k_{i,1} & \cdots & k_{i,j} \end{bmatrix} \quad (33)$$

After obtaining the global stiffness matrix, the natural frequencies could then be determined for the structure using equation 34 (Craig & Kurdila, 2006).

$$w_n = \sqrt{\frac{M}{K}} \quad (34)$$

Where w_n, M, and K is the natural frequency, mass matrix, and stiffness matrix respectively. This can be solved utilizing an eigenvalue analysis shown in equation 35 (Craig & Kurdila, 2006).

$$[K]\{x\} = {w_n}^2[M]\{x\} \quad (35)$$

Where {x} is the eigenvectors. The natural frequencies are sorted and given in Table 5.1.1. These values are also compare to the natural frequency's obtained from the truss using the CPSD method.

Table 5.1.1 Natural Frequency Comparison between the Truss and the MATLAB Model

Mode	MATLAB Natural Frequency (Hz)	Truss Natural Frequencys (Hz)	Error (%)
1	13.21	9.88	33.70
2	14.17	18.31	-22.61
3	29.58	26.73	10.66
4	39.98	32.84	21.74
5	45.71	34.55	32.30
6	53.53	50.29	6.44

As shown, there is a large amount of error when comparing the natural frequencies of the lab scale truss and the numerical model truss. This could be due to many reasons, including uncertain geometric stiffness for each element of the lab scale truss, due to possible torque difference applied in assembly or intrinsic damping that is not accounted for in the natural frequency equation. Because of this error, model updating was performed to optimize the results.

5.2 Model Updating

To obtain more accurate results, model updating was performed. Model updating is the procedure for which a given model gets updated to more accurately reflect the real-life structure that is being modeled. This can be done by slightly adjusting some of the assumed parameters associated with the structure.

Various properties could be changed to best estimate the bridge response. However, the modulus of elasticity for the nylon rope was adjusted. This is because the rope was assembled with some variability in the tension of each rope element. Because of this, the modulus of elasticity was reduced to reflect the reduction in strength. the modulus of elasticity was changed from 435,000 psi to 100,000 psi. This then gave more accurate natural frequency values as shown in table 5.2.1.

Table 5.2.1 Updated Natural Frequency Values

MODE 1	MATLAB Natural Fequency (Hz)	Truss Natural Frequncy (Hz)	Error (%)
1	9.74	9.88	-1.42
2	16.52	18.31	-9.78
3	24.48	26.73	-8.42
4	34.39	32.84	4.72
5	36.76	34.55	6.40
6	45.67	50.29	-9.19

As shown, the natural frequencies obtained from the finite element model are a closer match to the natural frequencies obtained for the lab-scale bridge. This is evident as all the error is within 10% compared to having error within 30% originally. The error still looks large; however, we decided to use current status as the Kalman Filter can accommodate uncertainty in modeling in some degree by adjusting system error covariances.

5.3 Mode Shape after Model Updating

The first six modes were analyzed to compare to the mode shapes of the truss structure. Modes 2 and 6 were the non-torsional modes that occurred, which matches the mode shapes obtained using the peak-picking method for the truss.

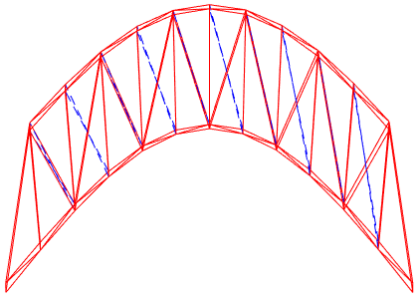

Figure 5.3.1 1ST Bending Mode Shape Using MATLAB

Mode 2 shown is the first bending mode shape to occur. The largest displacement is in the center of the truss whereas the ends receive minimal displacement. This matches the mode shape that was determined using SAP2000 and the mode shape determined using the peak-picking method for the truss. Furthermore, the truss looks to be smooth, as not one side is experiencing any sort of torsional forces acting on it.

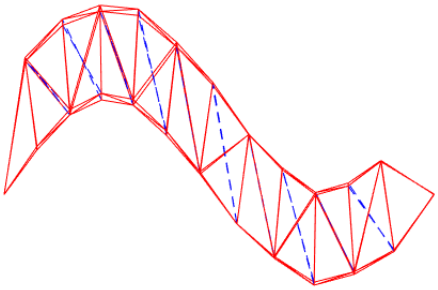

Figure 5.3.2 2nd Bending Mode Shape Using MATLAB

Mode 6 is the second bending mode to occur. The largest displacements are at the quarter points whereas the midpoint has negligible displacement. This matches the SAP2000 model mode shape and the actual truss mode shape. Both bending mode shapes determined using MATLAB are accurate depictions of the lab scale bridge with similar matching natural frequency values.

The mode shapes were used to determine the damping for the structure. The damping is needed for the Kalman filter application. The damping matrix was determined using the modal damping method. This method uses the eigenvalues and eigenvectors to obtain a damping matrix, C, as shown in equation 36 (Craig & Kurdila, 2006). The benefit of this method is that this damping matrix is constructed for all modes of the structure.

$$C = \sum_{r=1}^{N} \frac{2\zeta_r w_r}{M_r} M\emptyset_r (M\emptyset_r)^T \tag{36}$$

Where N, r, ζ, are the number of modes, starting mode, and assumed damping coefficient. For this structure, it was assumed that damping coefficient equals 2%. Typical values for the modal damping factor range from 1% to 10%.

6. Model-based Structural Response Estimation

Two separate loading conditions were performed to obtain strain and acceleration responses along predetermined few locations of the truss. These measurements were input in the Kalman filter to obtain strain values across the whole structure.

6.1 Strain Estimation for the Impact Force Excitation

For the impact force test, four separate cases, each with a different sensor arrangement and sensor number, were considered for the Kalman filter to determine the optimal number of sensors used and maximum strain estimated. For this test, the strain was estimated for element 122, where strain gage 2 (see Figure 6.1.1) is located, for validating the Kalman filter algorithm. Case 1 only uses one strain gage located on element 3. Case 2 uses the accelerometers located on nodes 4, 13, and 20 in addition to one strain gage on element 3. Case 3 uses accelerometers located on nodes 4, 13, 16, 18, 20, and 21 with one strain gage located on element 3. Case 4 uses more numbers of accelerometers located on nodes 4, 9, 11, 13, 15, 16, 18, 20, and 21 with the one strain gage located on element 3.

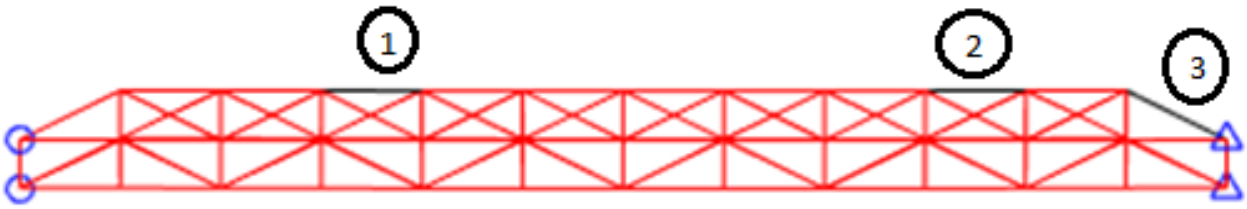

Figure 6.1.1 Strain Gage Locations

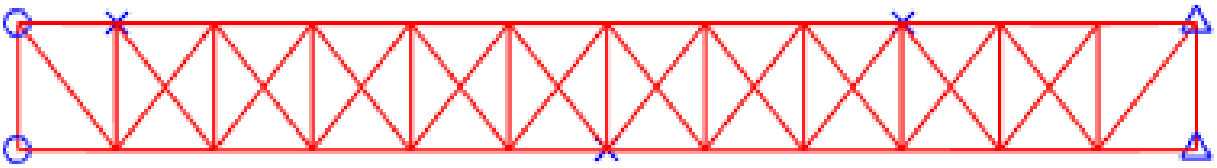

Figure 6.1.2 The 3 Accelerometer Locations for Case 2

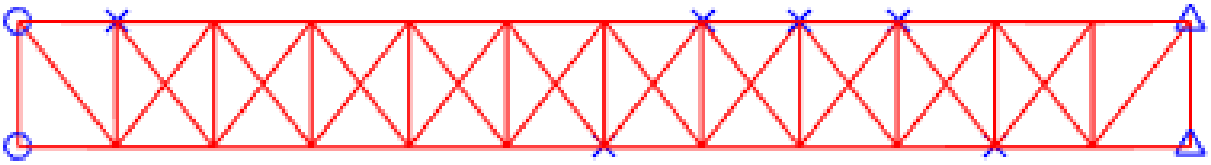

Figure 6.1.3 The 6 Accelerometer Locations for Case 3

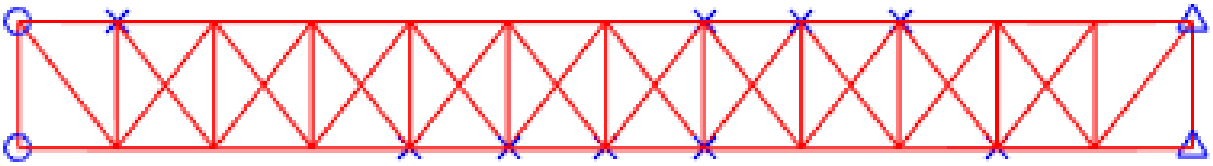

Figure 6.1.4 The 9 Accelerometer Locations for Case 4

For Case 1, only the strain gages were used when performing the Kalman filter approximation. As shown in Figure 6.1.5, there is an accurate correlation between the measured data (blue) and estimated data (red). The estimated data generates more noise, however, the peak values estimated are at the same location with roughly the same amplitude. The maximum estimated strain for element 122 is 6.82e-5. This is smaller than the maximum measured strain of 1.17e-4.

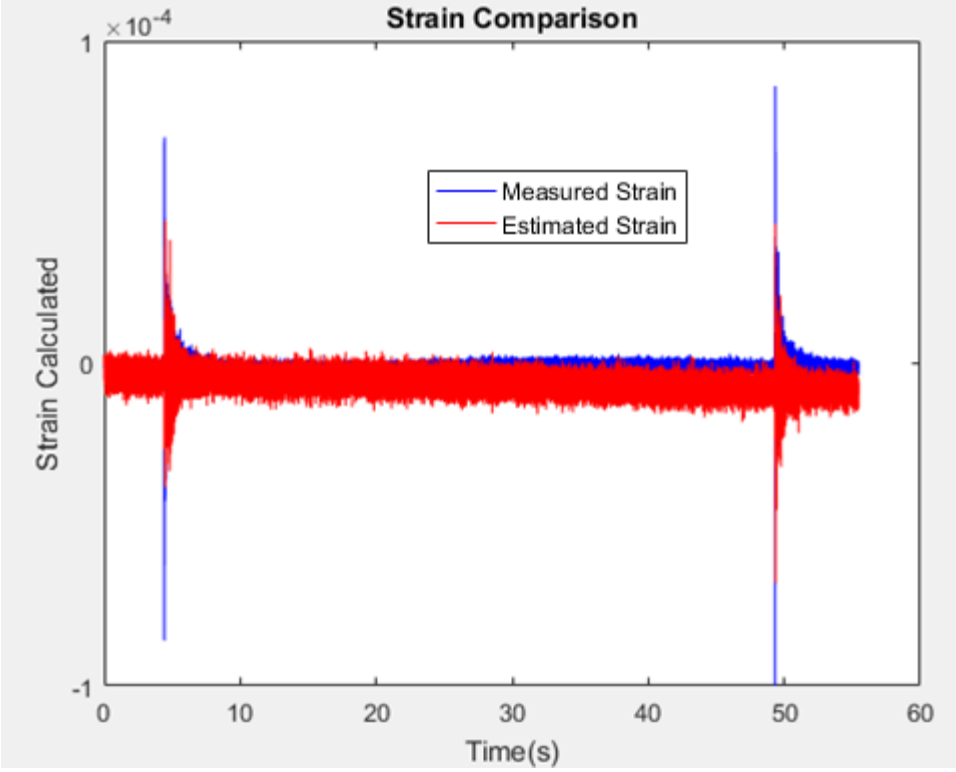

Figure 6.1.5 Strain Estimated for Case 1

The maximum strain was estimated for all elements as well. As shown in Figured 6.1.6, Element 128 (black) was determined to be the element with the maximum strain estimated. The strain estimated is 1.33e-4. This value is largest due to the proximity of the member to the node with the applied loading condition.

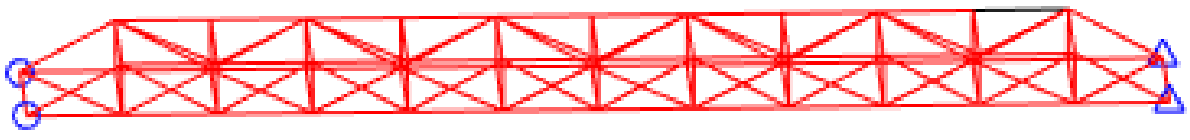

Figure 6.1.6 Maximum Strain Measured Location for Case 1

Case 2 uses the one strain gages and three accelerometers for the Kalman Filter estimation. Figure 6.1.7 shows the strain estimated for Case 2.

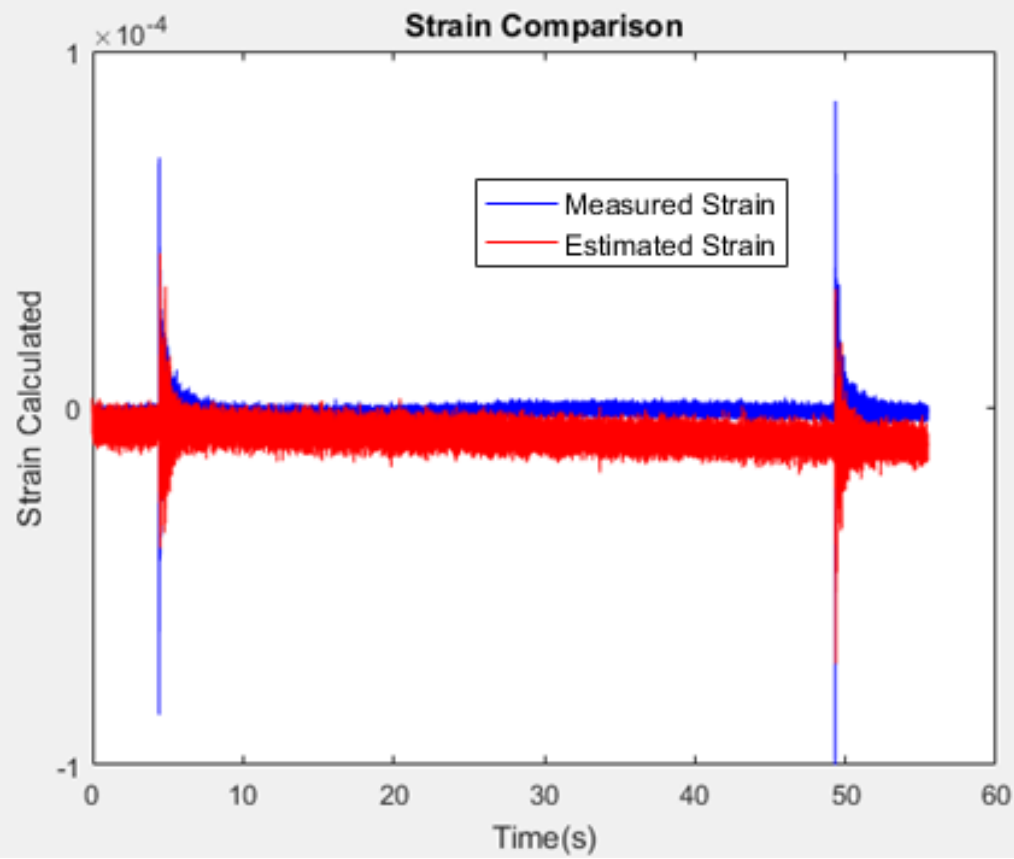

Figure 6.1.7 Strain Estimated for Case 2

As shown, the estimated strain closely matches the measured strain. The estimated peaks are at the same locations as the measured peaks. Along with the previous case, the amplitudes of the estimated peaks are not as large as the estimated peaks. A downward trend starts to occur near the end. The maximum strain measured for element 122 is 7.18 e-05. This is closer than Case 1 to the measured strain value of 1.17e-04. As shown in Figure 6.1.8, the maximum estimated strain for the whole truss occurs on element 128 (black) and is 1.18e-04.

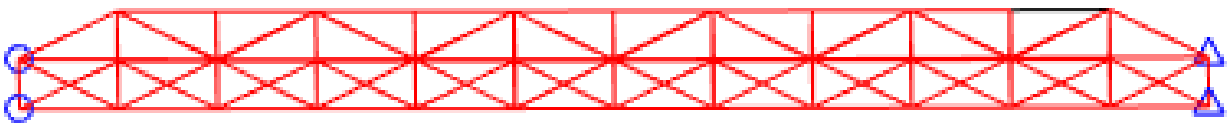

Figure 6.1.8 Maximum Strain Measured Location for Case 2

Case 3 uses the one strain gage and 6 accelerometers for the Kalman Filter estimation. The maximum strain measured for element 122 is 9.19e-05. This value closer to the measured strain value of 1.17e-04. As shown in Figure 6.1.9, the estimated strain does not have as large of a negative trend as shown in Cases 1 and 2. The locations of the peaks for the estimated data (red) also match with the locations of the peaks for the measured data (blue).

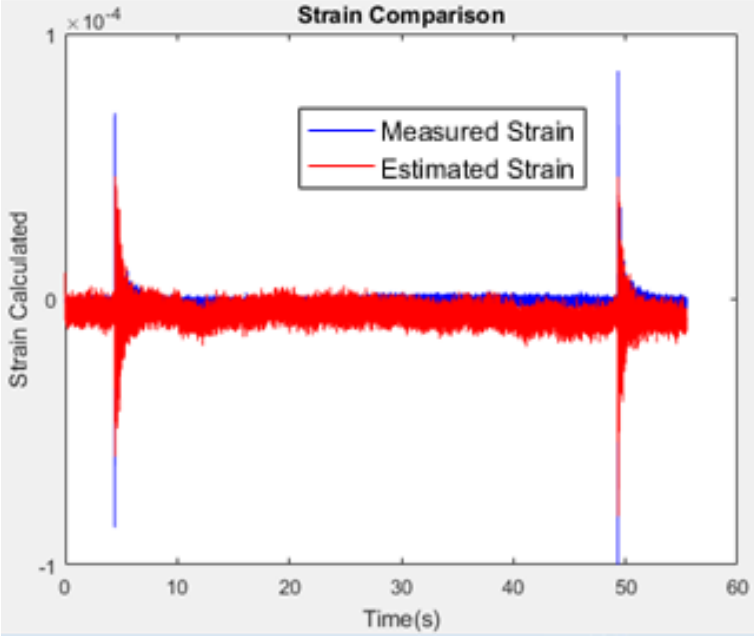

Figure 6.1.9 Strain Estimated for Case 3

The maximum strain estimated for the whole truss is located on element 128 (black) as shown in Figure 6.1.10. This location is different from Cases 1 and 2 as it is on the element with maximum strain as predicted using the SAP2000 analysis. A larger number of sensors used in the Kalman Filter increases the accuracy of this estimation technique.

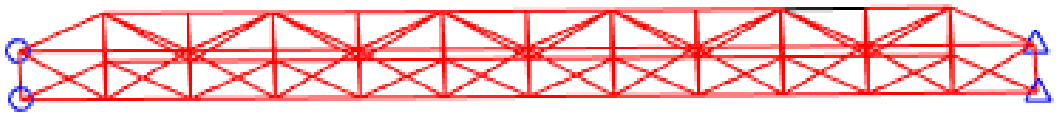

Figure 6.1.10 Maximum Strain Measured Location for Case 3

Case 4 was ran was using the one strain gage and 9 accelerometers. As shown in Figure 6.1.11, the strain estimated is consistent with the strain measured. The estimated strain peak is located at the same time as the measured strain peak. The maximum strain measured for this gage combination is 9.15e-05, which is close to the 1.17e-05 that was measured. Case 4 has a lower strain estimation that case 3 but a higher strain estimation than case 1 and 2. No other sensor combinations were ran afterwards because case 4 did not have a larger estimated strain response than case 3.

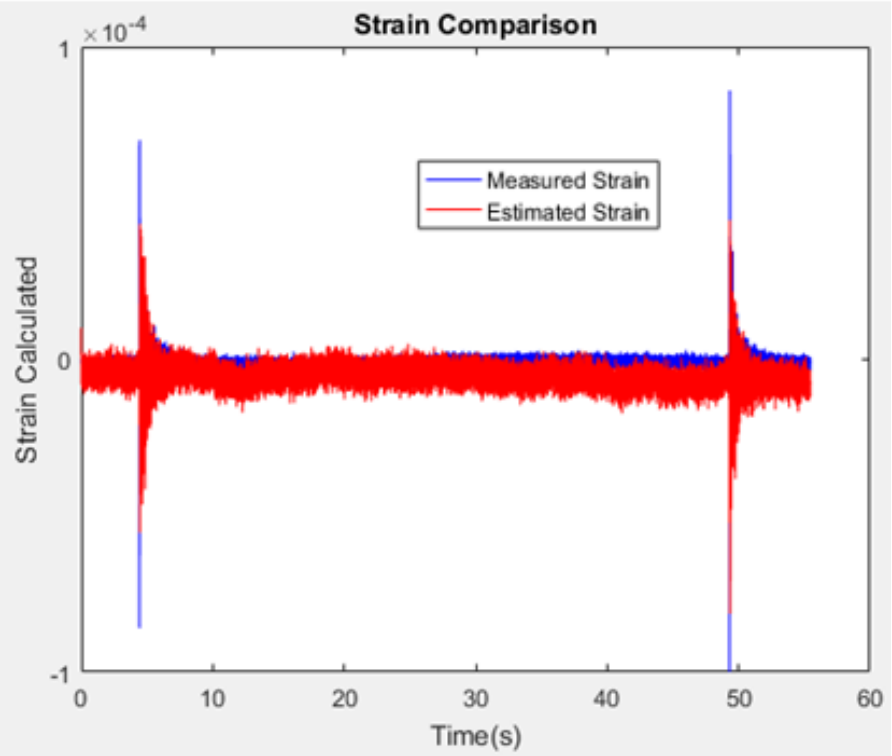

Figure 6.1.11 Strain Estimated for Case 4

As shown in Figure 6.1.12, the maximum strain across the whole truss was estimated to be on element 122. This is the element for which the SAP2000 model predicted to experience the largest strain for this loading condition.

Figure 6.1.12 Maximum Strain Measured Location for Case 4.

The maximum strain measured was compared with the number of sensors used. As shown in Figure 6.1.13, the strain estimated was generally more accurate when using more sensors. This is because the more strain gages and accelerometers used, the better prediction will occur through the Kalman filter. However, after using 8 sensors, the trend starts to decline. This suggests that an optimal number of sensors can be used, as using too many may lead to conversion at a certain point without much improvement.

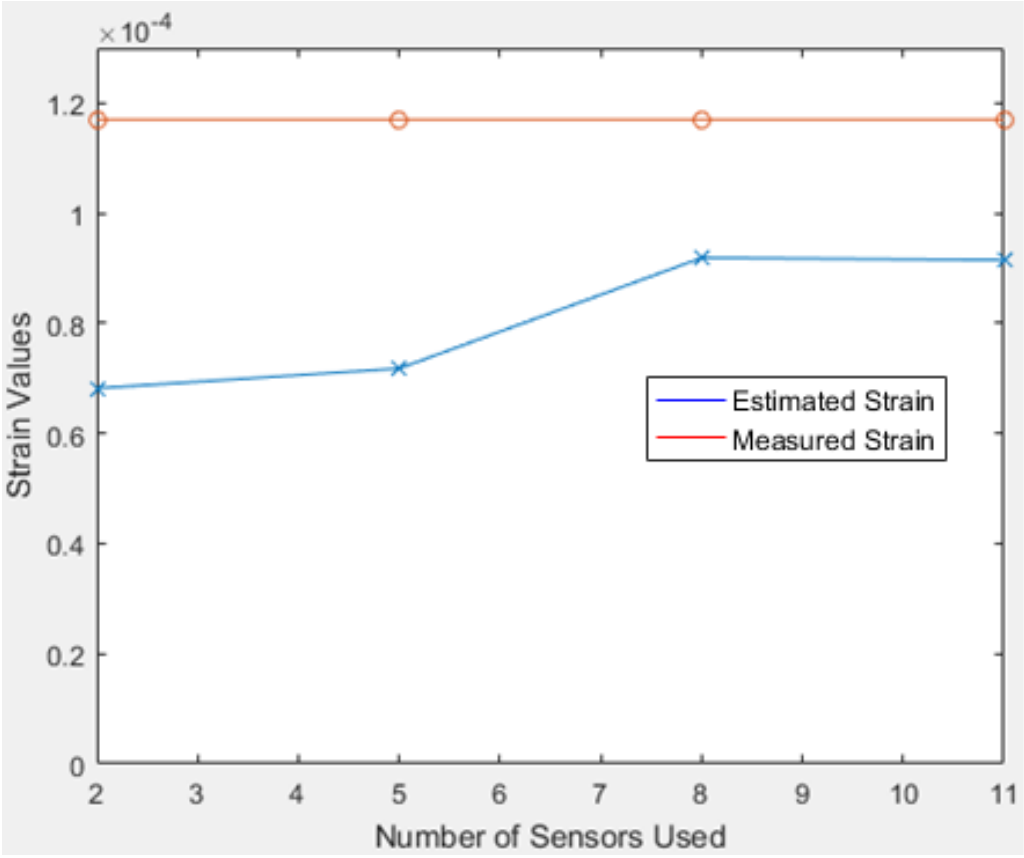

Figure 6.1.13 Number of Sensors vs Maximum Estimated Strain

6.2 Strain Estimation for the Random Excitation Test

The second loading condition is the random excitation test. For this test, the strain was estimated at two strain gage locations as shown in Figure 6.2.1. 3 separate cases, with different accelerometer locations, were ran through the Kalman Filter for each strain gage location. Case 1 uses only one strain gage for the Kalman Filter. Case 2 uses one strain gage and three accelerometers for the Kalman Filter. Case 3 uses one strain gage and 6 accelerometers. The accelerometers locations for cases 2 and 3 correspond to the accelerometers locations in Figure 6.1.2 and 6.1.3, respectively. A low pass filter was applied at 500Hz to help filter the data.

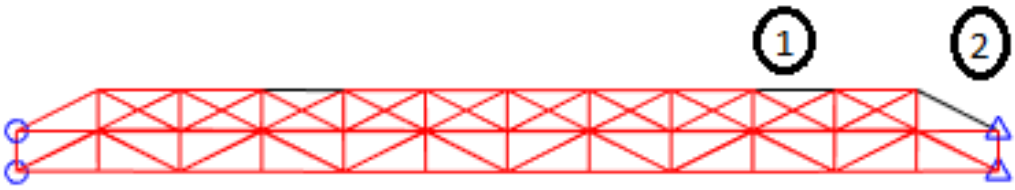

Figure 6.2.1 Strain Gage Locations Used in the Kalman Filter

When analyzing the first strain gage, the estimated vs the measured strain data was compared. The red strain data is the estimated data whereas the blue strain data is the measured data. The estimated data has a large amount of noise. However, the peak locations of the graphs are matching. The maximum strain estimated is 2.72e-05 which is close to the measured strain value of 3.03e-05.

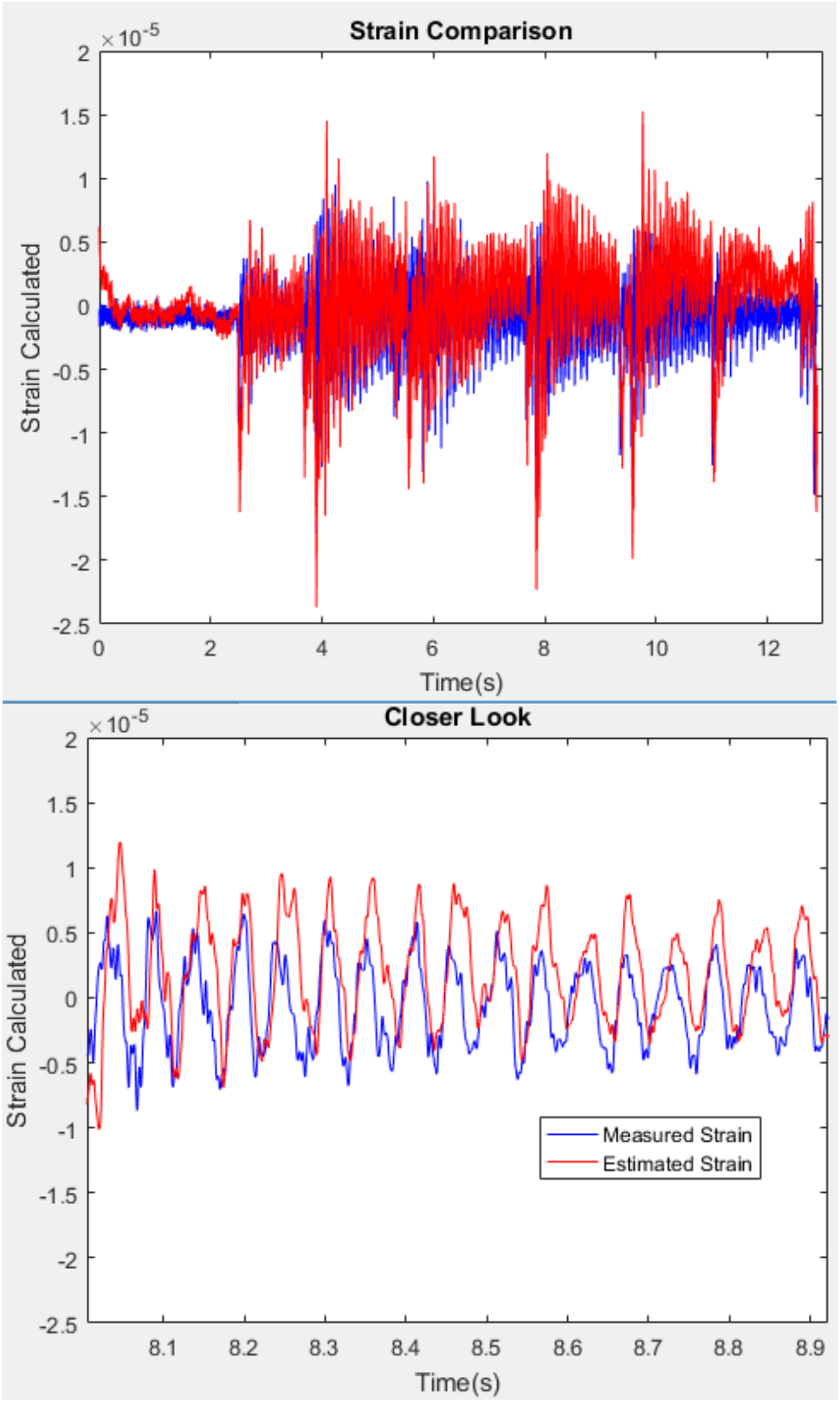

Figure 6.2.2 Strain Gage 1 – Case 1

When using 4 gages for Case 2, the results were more accurate. As shown in Figure 6.2.3, the estimated data of the peaks matches closely to the measured data's peaks. The maximum strain estimated is 2.79e-05 which is closer to the 3.03e-05 value measured than in Case 1.

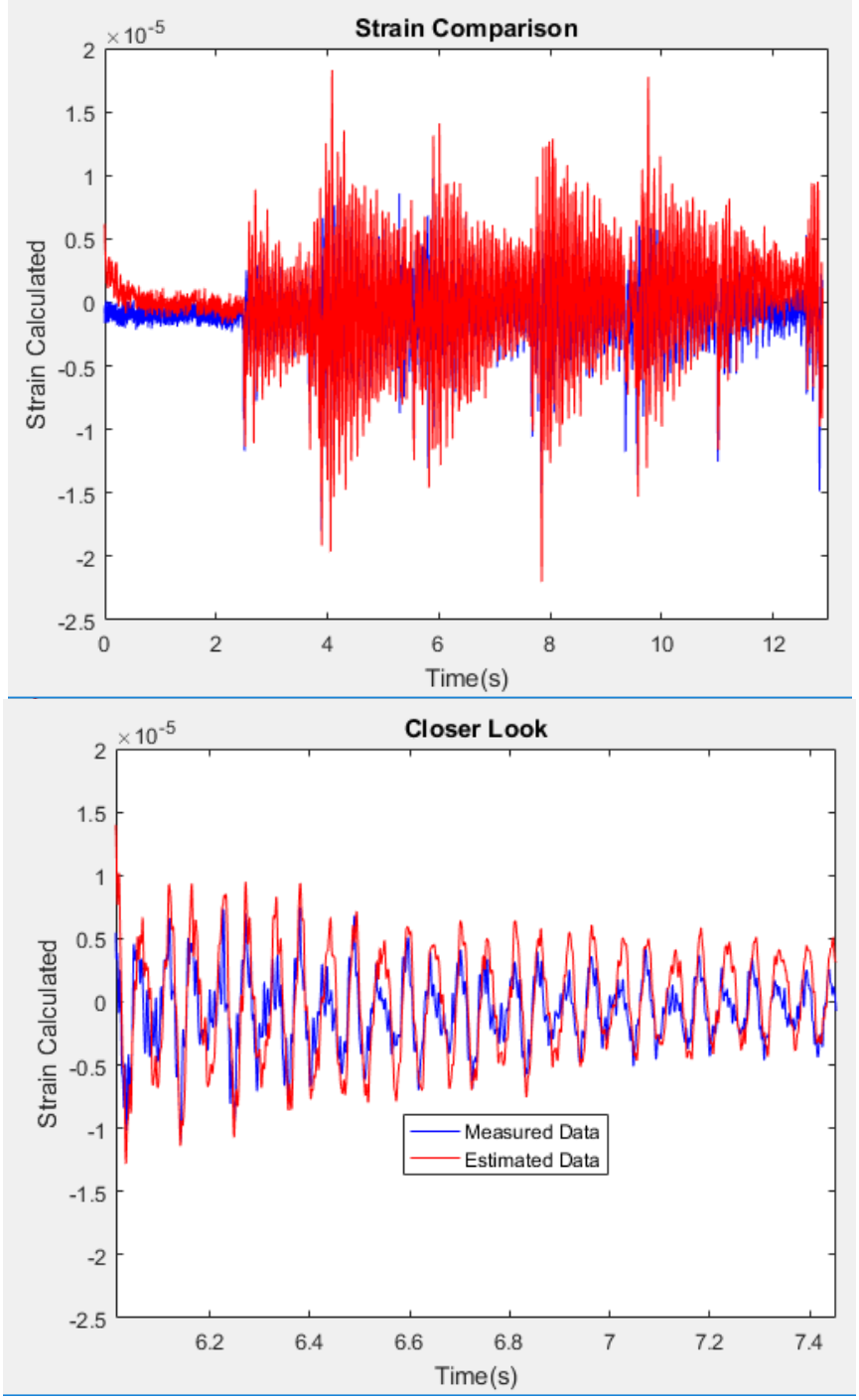

Figure 6.2.3 Strain Gage 1 – Case 2

When 7 gages are used for Case 3, more accurate results were obtained. The estimated results match closely to the measured results. This is evident as the estimated peaks and measured peaks lineup. For this case, the maximum strain estimated is 2.86e-05. This is even closer to the measured value of 3.03e-05 than cases 1 and 2.

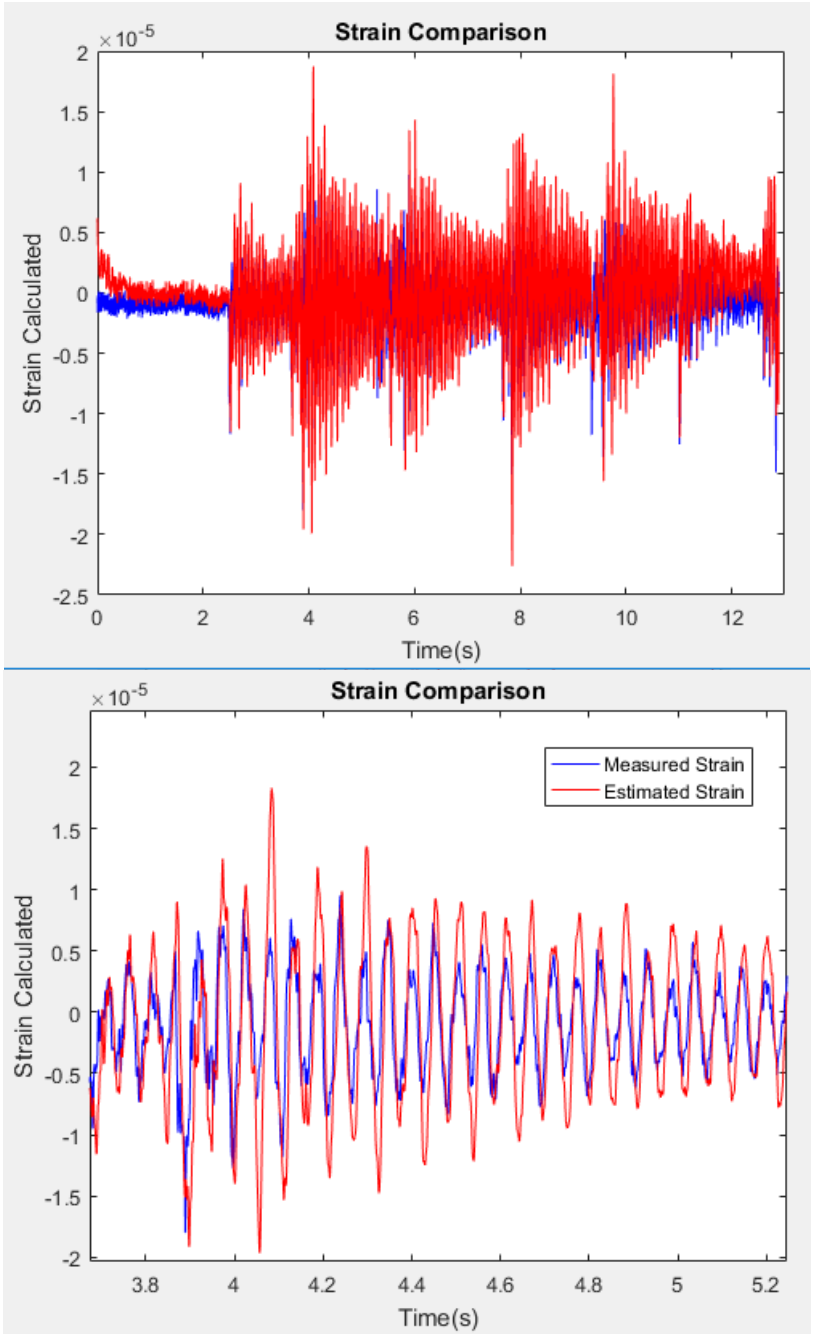

Figure 6.2.4 Strain Gage 1 – Case 3

After getting accurate results with 7 gages, the strain at sensor location 2 was then estimated using the same approach. After running the simulations, the estimated strain data for location 2 is not as accurate as the estimated data for location 1. The strain peak locations are not as aligned as they were for location 1. Furthermore, the estimated strain values are smaller than the measured strain values. For Case 1, the maximum strain estimated is 1.57e-05 whereas the maximum strain measured is 1.98e-05.

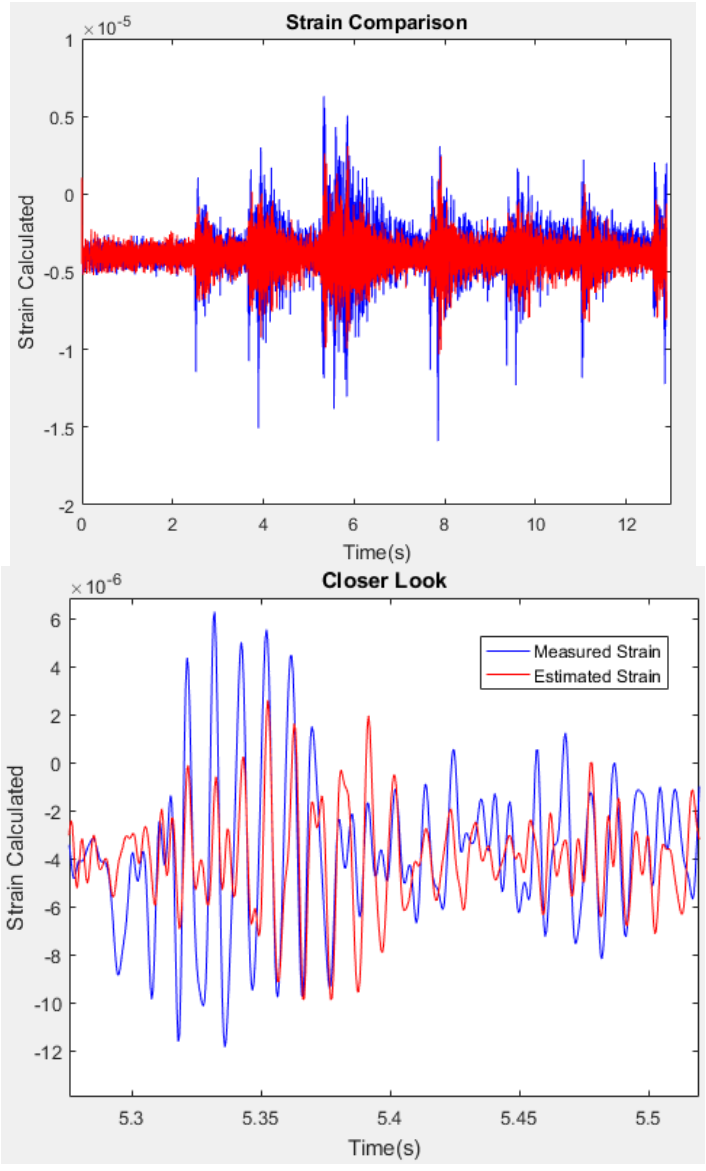

Figure 6.2.5 Strain Gage 2 – Case 1

When 4 sensors were used for Case 2, the results were only slightly better. As shown in Figure 6.2.6, the strain data estimated peaks match the strain measured peaks, however, the estimated peaks amplitude is smaller than the measured peaks amplitude. Furthermore, the peaks do not align as nicely as the peaks for location 1 did. The maximum strain estimated is 1.58e-05, which is closer to the measured value of 1.98e-05 than Case 1.

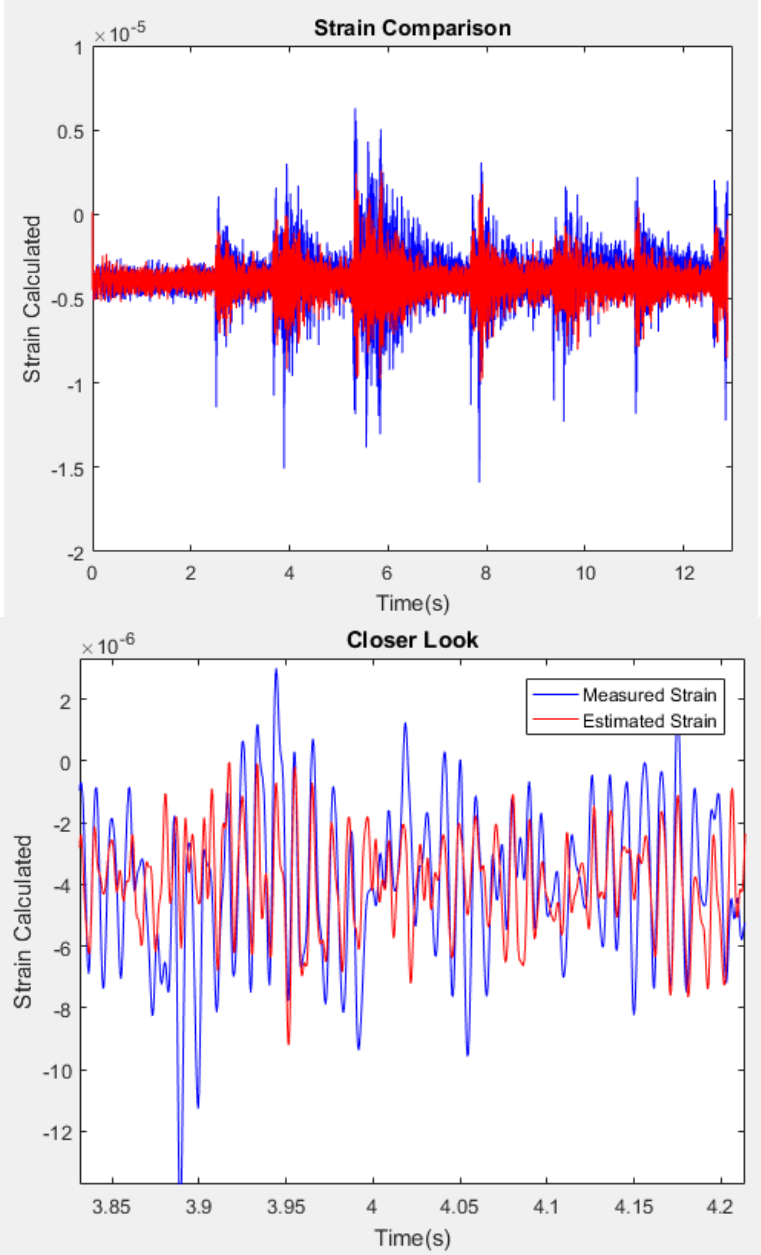

Figure 6.2.6 Strain Gage 2 – Case 2

When using 7 gages for Case 3, the results were nearly identical to the results for Case 2 and 1. The estimated data aligns with the measured data, however, the amplitudes for the peaks in the estimated data are smaller than the amplitudes for the peaks in the measured data. Furthermore, the estimated maximum strain estimate is 1.58e-05, which is the exact same as using only 4 gages for the Kalman filter. This suggests that increasing the number of sensors used does not increase the accuracy of the Kalman Filter after reaching the optimal number of sensors.

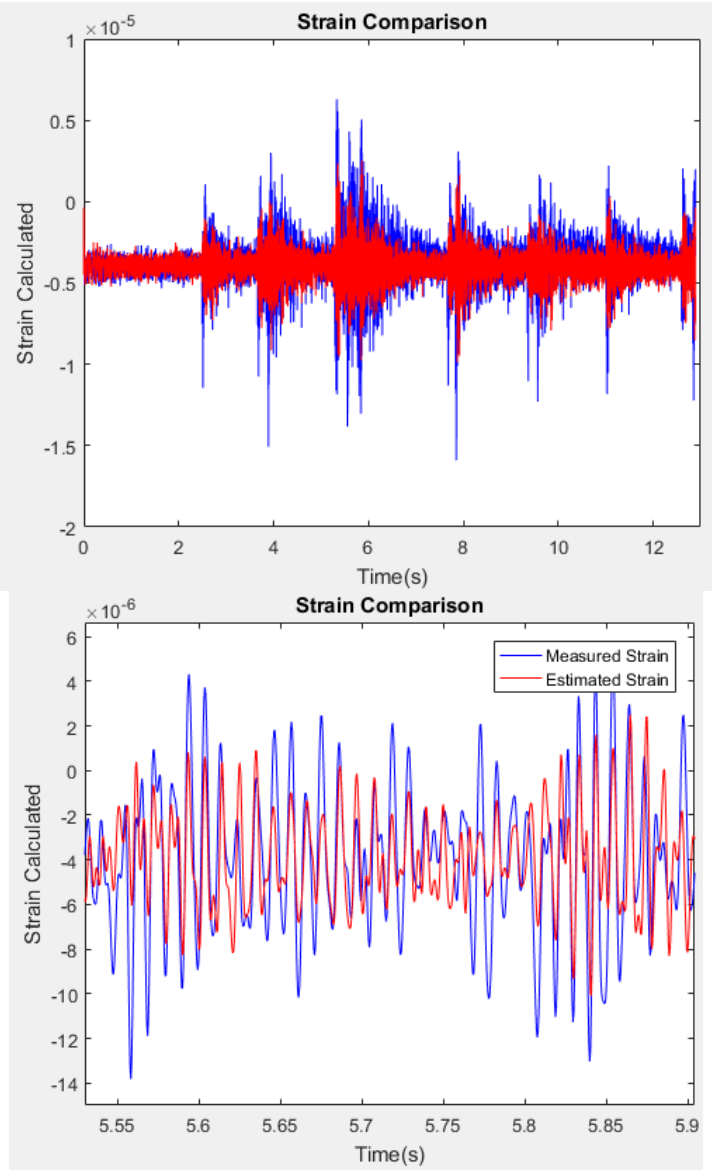

Figure 6.2.7 Strain Gage 2 – Case 3

The strain data obtained from estimating strain location 1 had a better correlation with the measured data then the strain data obtained from estimating strain location 2. As shown in Table 6.2.1, it can be shown that increasing the number of sensors for strain location 1 had a positive correlation for decreasing the error whereas strain location 2 has no correlation. This suggests that more gages should be used in the Kalman Filter approach to obtain more accurate results. However, an optimal number of sensors is needed for this. Along with this, an optimal sensor location should be considered for best results. This could decrease the error shown for strain gage 2.

Table 6.2.1 Strain Error Estimation

Strain Data				
Strain Gage Analyzed	Sensors Used	Strain Measured	Strain Estimated	Error
1	1	3.03E-05	2.72E-05	-10.23%
	4	3.03E-05	2.79E-05	-7.92%
	7	3.03E-05	2.86E-05	-5.61%
2	1	1.98E-05	1.57E-05	-20.71%
	4	1.98E-05	1.58E-05	-20.20%
	7	1.98E-05	1.58E-05	-20.20%

The error obtained from the random excitation test is minimal compared to the error obtained from the impact load test. This is because the Kalman filter approach is more suited for random vibrations over a periodic loading. This makes this approach ideal for monitoring bridges, as the traffic loads may be close to random vibration loading conditions in long terms. The maximum error obtained in strain gage 1 was 10.23% but was reduced to 5.61% when more sensors were used. The maximum error obtained in strain gage 2 was 20.71% but was reduced slightly to 20.20% when more sensors were used. All the strain values estimated were slightly lower than the values measured. This suggests that more strain gages are needed to obtain the strain data from other elements of the bridge.

7. Live load Performance Index Determination

The strain data estimated using the Kalman Filter for entire structural elements was used to calculate the Live Load Performance Index. Two example cases were used to demonstrate the use of this index. For the first case, the maximum strain estimated over time was used to determine a critical LLPI value for every member of the truss. This scenario was done for both the random excitation and the impact force loading situations. For the second case, a single element was analyzed over time and a LLPI variation was generated for every strain value estimated over the time.

7.1 LLPI for Maximum Strain Estimated

The maximum strain estimated from case 3 was used to determine the LLPI for the random excitation loading scenario. This was done as case 3 had the most accurate strain results out of all the cases. As shown in Figure 7.1.1, no values are less than one. This means that yielding has not started to occur in the members for this particular random loading. Furthermore, the minimum value is 5.4 and occurs on element 122. This element connects to the node where the force is applied, so the strain here will be the greatest, meaning the LLPI will be the smallest, which may represent the most critical LLPI for whole structure. Most values are in the range of 10-50 LLPI. These values are relatively large because the force being applied is relatively small.

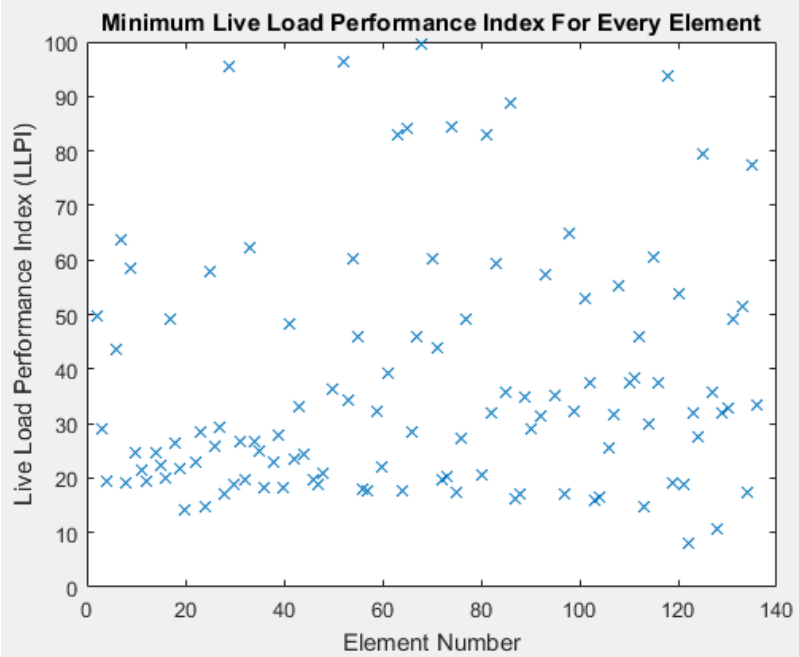

Figure 7.1.1 LLPI Using the Maximum Strain Estimated for the Random Excitation Loading

The maximum strain estimated for the impact force loading condition was also used to determine a LLPI. The maximum strain used for this scenario was taken from Case 4. This was done as Case 4 had the most accurate strain estimation results out of all the cases. For this situation, all values are above one as well as shown Figure 7.1.2. However, the performance index values are a lot smaller than the ones calculated for the random excitation loading condition. This is because the strain values estimated from the Kalman Filter for the impact loading condition are larger, as a larger force was applied. The smallest index value measured is 2.3 and is on element 122 as well. This is the element with the maximum strain estimated in both the Kalman Filter approach and SAP2000 analysis. Most values are in the range of 5-10. This range is acceptable for the loading condition presented.

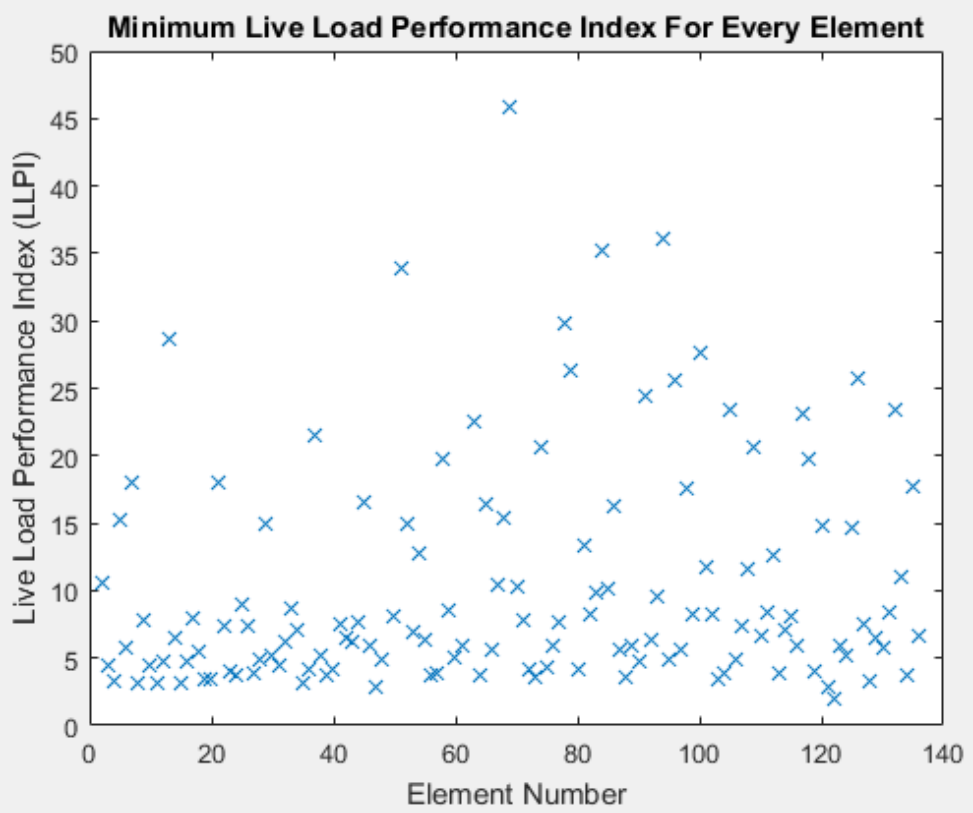

Figure 7.1.2 LLPI Using the Maximum Strain Estimated for the Impact Force Loading

7.2 LLPI variation For Member 122 Over Time

A performance index was determined over time for an individual member. Because member 122 was the member estimated with the largest strain, this member was used to estimate the LLPI variation over time as a example. This was done for both loading conditions as well. For the random excitation loading, a performance index was determined for every strain value over the 13 second interval. As shown in Figure 7.2.1, all values are above one as well. There are multiple peaks shown when the loading was occurring. The minimum LLPI calculated for this condition is

15.3. The peak values are between the range of 10 and 30. This is acceptable for the loading applied.

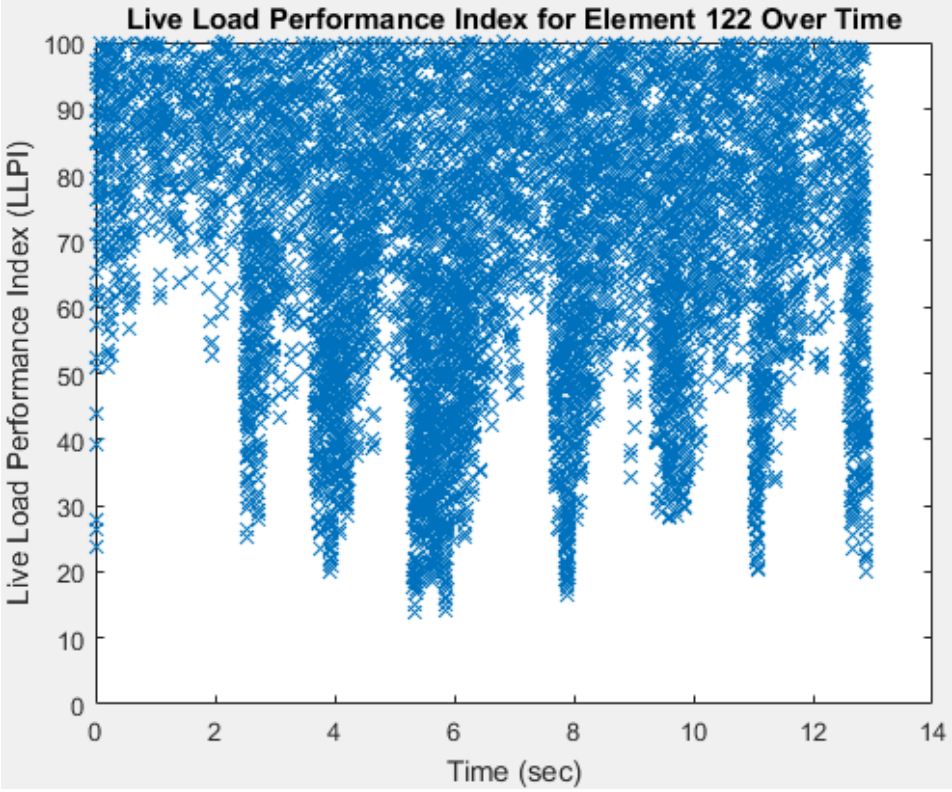

Figure 7.2.1 LLPI for the Random Excitation Loading for Element 122 Over Time

As opposed to the LLPI obtained by the random excitation scenario, the LLPI obtained from the impact force scenario is lower. As shown in Figure 7.2.2, there is only one peak, which is located at the same time when the hammer was hit on the node. The minimum rating index for this loading situation is 3.8. All other values are extremely large an are due in part to the noise received from the sensors. This is acceptable for the loading applied.

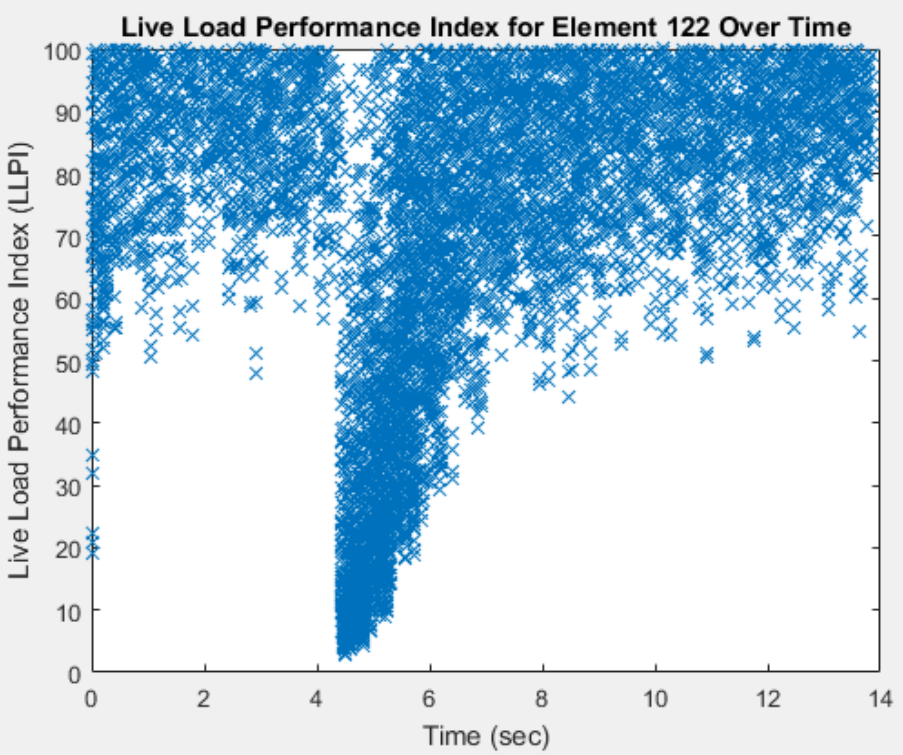

Figure 7.2.2 LLPI for the Impact Force Loading for Element 122 Over Time

8. Conclusions

The current bridge load rating process does not account for structural condition changes in between the load rating timeline. Along with this, the load rating procedure has too many limitations in order for it to be an effective way to estimate the capacity of a bridge.

A new Live Load Performance Index (LLPI) is created which determines the live load capacity that the bridge can withstand. This is a continuously monitoring effort, which allows it to be effective in between the bridge rating period. Furthermore, this method utilizes the strain data obtained from sensors to better estimate the capacity of the bridge, rather than visually inspecting the structure. This method follows the same approach as the traditional bridge load rating formulation while determine the LLPI, except it uses the actual and real-time strain responses from a live load to estimate the LLPI variation over time instead of design live load. The strain is estimated using the augment Kalman Filter using limited number of sensors, which requires a combination of experimental data and numerical modeling.

Experimental measurements were obtained by placing strain gages and accelerometers throughout the structure. The locations for these was determined using a SAP2000 analysis of the truss structure. A unit point load was applied to a singular node on the truss in order to predict the strain at every location using basic mechanic of materials. This analysis was also used as a reference when performing system identification on the lab-scale truss.

The truss was used to run two different experiments, a random excitation loading condition and an impact force loading condition. The data obtained from both tests was the strain and acceleration. The acceleration data from the random excitation test was used for system identification of the truss. Cross power spectral density was performed in order to determine the natural frequency's and mode shapes. The first 6 modes were analyzed and corresponded accurately with the mode shapes obtained from the SAP2000 Analysis.

A numerical model was made in MATLAB so that a state-space representation, which is needed for the Kalman Filter, could be made. The mass, stiffness, and damping matrices were obtained using finite element methods for each. The mode shapes and natural frequencies were determined and matched those that were obtained for the lab-scale truss. However, model updating was performed to reduce some error involved.

The strain was estimated using the augmented Kalman Filter across the entire truss structure. This was done for both loading conditions. The random excitation loading condition experienced more accurate results as less error was obtained. However, the maximum strain location could be accurately determined for both situations. Furthermore, the strain peak locations were accurately estimated for both cases using the Kalman Filter.

The Strain data obtained using the Kalman filter was then used to create the Live Load Performance Index (LLPI) for different situations. The was calculated for two different conditions. the first condition was using the maximum strain for every element to determine the minimum

LLPI for the entire Truss. The second condition was using examining a singular element and calculating the LLPI for every strain value estimated over the given time frame. Both conditions resulted in an accurate depictions of the live load performance that the truss could withstand.

8.1 Area of future work

The strain gages and accelerometers were placed on the truss structure according to an initial SAP2000 Analysis. The number of sensors used and sensor locations was solely based on areas that should receive a large amount of strain. An optimization algorithm should be written in order to accurately predict how many sensors should be placed and where they should be placed at. This can be done using a generic algorithm, as this is a simple and quick approach. In addition to this, a generic algorithm can be written in order to optimize which sensors to use for the Kalman Filter. This will eliminate the need for repetitive cases and was presented in this thesis. Furthermore, an optimization algorithm can be written for the Kalman Filter covariance variables as well. These had to be changed every for every case and eliminating this would save time while also decreasing the error involved.

Currently, this paper proposes a template that would be able to describe a real-life bridge. By validating that a bridge in a controlled environment can accurately determine a LLPI, one can then try this approach on bridge that experiences traffic. The next step would be to compare the calculated LLPI for a large-scale bridge that experiences traffic load. The procedure and setup would be the same as outlined.

9. References

AASHTO. (2011). Section 8: Nondestructive Load Testing. In *Manual for Bridge load Rating*.

ADOT. (2011). Bridge Load Rating Guidelines

Bad bridges: Federal data shows US infrastructure crumbling. (2014). Retrieved August 01, 2017, from https://www.rt.com/usa/246041-deficient-bridges-usa-infrastructure/

Bridge design practice. (2015). Sacramento, CA: Caltrans.

Colorado. (2012). Lumped and Consistent Mass Matrix. Retrieved July 31, 2017, from http://kis.tu.kielce.pl//mo/COLORADO_FEM/colorado/IFEM.Ch31.pdf

Craig, R. R., & Kurdila, A. J. (2006). *Fundamentals of structural dynamics* (2nd ed.). New York: John Wiley & Sons.

Desai, C. S., & Kundu, T. (2001). *Introductory finite element method*. Boca Raton, FL: CRC Press.

Gavin, H. P. (2014). *The Matrix Stifness Method for 2D Truss*. Duke University.

Greene, B. (2013). Bridge Load Rating Utilizing Experimental Data and Finite Element Modeling.

GPA: D. (2017). Retrieved August 01, 2017, from http://www.infrastructurereportcard.org/

Hibbeler, R. (2006). *Structural analysis*. Upper Saddle River: Pearson Prentice Hall.

L. (2001). Manual for Condition Evaluation and Load Rating of Highway Bridges Using Load and Resistance Factor Philosophy. *NCHRP*.

Melvin, D. (2016). Model based approach for structural monitoring of plate structures using the Kalman filter .

McMaster-Carr. (n.d.). Retrieved August 01, 2017, from http://www.mcmaster.com/

National Instrument. (2016). Understanding FFT's and Windowing.

Online Materials Information Resource - MatWeb. (n.d.). Retrieved August 01, 2017, from

http://www.matweb.com/

Paulo R Rogerio, et al. “Paulo R Rogerio.” *Go to National Precast Concrete Association.*, 28 July 2010, precast.org/2010/07/hl93-truck-loads-vs-hs20-truck-loads/. Accessed 20 Sept. 2017.

Rowell, D. (2002). State Space Representation of LTI Systems. *Analysis and Design of Feedback Control Systems*. Retrieved March & april, 2017.

Samali, B. J. (2007). Load Rating of Impaired Bridges Using a Dynamic Method. *EJSE International*.

Sanayei, M., & Dicarlo, C. (2009). Finite Element Model Updating of Scale Bridge Model Using Measured Modal Response Data. *Structures Congress 2009*. doi:10.1061/41031(341)11

SAP2000: integrated software for structural analysis and design. (2006). Berkeley Calif.: CSI.

Sim, S. H. (2014). Experimental Validation of Strain Estimation Using Model-Based Kalman Filter for Multi-Sensor Fusion.

Student Dave's Tutorials. (n.d.). Retrieved September 20, 2017, from http://studentdavestutorials.weebly.com/

Texas Department of Transportation. (2013). *Bridge Inspection Manual*. Texas.

Welch, G. (2006). An Introduction to the Kalman Filter.

Zhang, Y. X. (n.d.). Finite Element Model Updating of a truss model using incomplete modal data.

http://onlinemanuals.txdot.gov/txdotmanuals/ins/ins.pdf

http://aboutcivil.org/aashto-hl-93-loading-design.html